# Resource Allocation for Multi-Satellite Asynchronous Transmission in Integrated Communication and Navigation Networks

*Original*
Resource Allocation for Multi-Satellite Asynchronous Transmission in Integrated Communication and Navigation Networks / Wang, M., Wang, R., Ma, R., Kang, W., Liu, G., Meng, W.. - In: IEEE INTERNET OF THINGS JOURNAL. - ISSN 2327-4662. - 10:12(2025), pp. 14172-14187. [10.1109/jiot.2025.3526154]

*Publisher:*
IEEE

*Published*
DOI:10.1109/jiot.2025.3526154

This article has been accepted for publication in IEEE Internet of Things Journal. This is the author's version which has not been fully edited and content may change prior to final publication. Citation information: DOI 10.1109/JIOT.2025.3526154

# Resource Allocation for Multi-Satellite Asynchronous Transmission in Integrated Communication and Navigation Networks

Mingyi Wang, Ruisong Wang, Ruofei Ma, *Member, IEEE*, Wenjing Kang, Gongliang Liu, *Member, IEEE*, and Weixiao Meng, *Senior Member, IEEE*

***Abstract*—The advantages of Low Earth Orbit (LEO) satellite navigation in addressing the increasing demand for high-precision and universally accessible positioning have garnered widespread attention. Our work builds upon our previous development of the Zadoff-Chu non-orthogonal multiple access (ZC-NOMA) waveform for integrated communication and navigation (ICAN). Expanding on this foundation, we conceive the ICAN-oriented multi-satellite asynchronous transmission (ICAN-MSAT) framework, which allows users to concurrently receive communication and navigation signals from multiple satellites without synchronization, thus increasing communication flexibility and leveraging the geometric distribution and robust signals of LEO satellite constellations to enhance navigation performance. Within the ICAN-MSAT framework, we propose a novel multi-satellite asynchronous transmission oriented subcarrier and power allocation (MSASP) algorithm to manage mutual interference between communication and navigation components and inter-satellite interference (INSI) caused by asynchronous transmission, with the latter often overlooked in most existing work. Simulation results demonstrate that the proposed algorithm meets the performance requirements of both navigation and communication, achieving higher communication rates under the same navigation accuracy constraints compared to current benchmarks.**

***Index Terms*—Integrated communication and navigation (ICAN); LEO satellite navigation; Asynchronous transmission; Resource allocation.**

## I. INTRODUCTION

The Global Navigation Satellite System (GNSS), a cornerstone of modern space infrastructure, is instrumental in delivering global positioning services across various sectors. Operating predominantly at altitudes between 19,000 and 35,000 kilometers, GNSS satellites encounter significant signal strength attenuation during Earth-bound transmission, typically ranging from -133 dB to -122 dB [1]. This distance-induced weakening of signals is further exacerbated in urban and indoor environments. Factors such as multipath reflections and non-line-of-sight (NLOS) propagation, combined with low carrier-to-noise ratios, severely impair the reliability and accuracy of GNSS [2].

This situation necessitates the exploration of augmentative technologies to strengthen GNSS performance [3]–[5]. One such promising approach involves integrating Low Earth Orbit (LEO) satellites into the existing GNSS framework [6]–[8]. Orbiting closer to Earth, LEO satellites not only markedly improve signal reception strength, but also offer enhanced geometric accuracy [7] and faster convergence times [9], thereby providing a robust solution to enhance the accuracy and reliability of GNSS services, especially in environments where traditional GNSS faces challenges. However, the deployment of a dedicated LEO navigation constellation with global coverage would not only entail substantial logistical and infrastructural investment but also require a significant time commitment. Meanwhile, LEO broadband communication constellations are rapidly expanding. The total number of satellites, including those already operational and those planned, is expected to reach tens of thousands [10].

Consequently, the concept of integrated communication and navigation (ICAN) has emerged, aiming to integrate communication and navigation functionalities into a unified system [11], [12], thereby reducing deployment costs. It also seeks to leverage synergies between navigation and communication, e.g., time advance (TA) estimation [13], ephemeris transmission [7], and precise orbit determination [14].

Current research on ICAN primarily focuses on waveform design [15]–[18] and resource allocation within individual satellites [19]. However, there is a notable gap in studies addressing cooperative strategies among multiple satellites providing ICAN services, particularly under conditions of asynchronous transmission, i.e., the time difference of signals received by users from different satellites surpasses the cyclic prefix (CP) duration of orthogonal frequency division multiplexing (OFDM), which will cause a loss of orthogonality between the OFDM subcarriers, leading to out-of-band emission (OoBE) and resulting in severe inter-carrier interference (ICI) and inter-symbol interference (ISI) [20], [21].

In light of these considerations, we have developed the ICAN-oriented multi-satellite asynchronous transmission (ICAN-MSAT) system for LEO networks. This system enables communication user terminals (CUTs) to form concurrent, asynchronous connections with multiple satellites, ensuring

---

This work is supported by Shandong Provincial Natural Science Foundation (ZR2023MF001, ZR2020MF141,ZR2024QF140),the Key R&D Program of Heilongjiang Province (JD22A001), and the National Natural Science Foundation of China (61971156, 61801144). (Corresponding authors: Ruofei Ma, Gongliang Liu)

Mingyi Wang, Ruisong Wang, Ruofei Ma, Wenjing Kang, Gongliang Liu, and Weixiao Meng are with Department of Communication Engineering, Harbin Institute of Technology, China (e-mail: `elewmy@163.com`, `mathwrs@163.com`, `maruofei@hit.edu.cn`, `kwjqq@hit.edu.cn`, `liugl@hit.edu.cn`, `wxmeng@hit.edu.cn`).

flexible and reliable communication. Navigation user terminals (NUTs) can use ICAN waveforms from these satellites for positioning, requiring connections with at least four satellites. To efficiently manage resources and control interference, we introduce a novel multi-satellite asynchronous transmission oriented subcarrier and power allocation (MSASP) algorithm. This algorithm mitigates mutual interference between navigation and communication components, as well as inter-satellite interference (INSI) due to asynchronous transmission, optimizing system sum rate while ensuring positioning accuracy.

To the best of our knowledge, this is the first work to explore multi-satellite cooperative strategies for ICAN, especially in scenarios involving asynchronous transmission. The main contributions of our work can be summarized as follows:

- We conceptualize an ICAN-MSAT system based on the ZC-NOMA waveform, introduced in our previous work [22], for an ICAN network. This architecture enables multiple satellites to simultaneously provide navigation and communication services to NUTs and CUTs within a covered region. We propose a subcarrier and power allocation problem that aims to maximize the sum rate of CUTs while ensuring the positioning accuracy for NUTs and meeting the throughput demands for each CUT, all within the bounds of maximum permissible transmission power.
- We provide a comprehensive analysis of the various types of interference present in the ICAN-MSAT system, including mutual interference between communication and navigation signals, as well as INSI caused by asynchronous transmission. This analysis forms the foundation for proposing effective mitigation strategies to ensure stable communication throughput and accurate navigation performance in asynchronous transmission scenarios.
- We develop an MSASP algorithm for the ICAN-MSAT system, which decomposes the original problem into two sub-problems: power allocation (PA) and subcarrier assignment (SA). For power allocation, we apply the difference of concave (D.C.) functions approximation method [23] to transform the non-convex problem into a solvable convex one. For subcarrier assignment, we introduce a dual-stage adaptive matching for subcarrier assignment (DAMSA) algorithm. The first stage ensures stable matching, while the second stage resolves unmatched situations through a suboptimal algorithm. The proposed MSASP algorithm effectively balances the throughput needs of CUTs with the positioning accuracy demands of NUTs, confirming its suitability for the ICAN-MSAT system.

## A. *Related Works*

***LEO Navigation*** – The integration of LEO satellite constellations with GNSS is gaining significant attention due to the unique advantages of LEO constellations, such as stronger signals [7] and enhanced anti-jamming capabilities [24]. These developments promise to advance satellite navigation beyond traditional GNSS systems. The European Kepler Project [25] aims for centimeter-level orbit accuracy and rapid Precise Point Positioning (PPP) convergence by combining LEO and Medium Earth Orbit (MEO) satellites. Similarly, the American Pulsar Service by Xona [26] and the Chinese Centispace-1 project [27] are leading efforts in high-precision positioning services with advanced small satellite technology. They focus on rapid PPP convergence and integrating broadband communication. Key challenges in LEO navigation, such as global coverage, ephemeris design, and clock synchronization, were discussed in [8], [28], [29], with [29] focusing on ephemeris design and [8], [28] providing an overview of these challenges.

***ICAN*** – The importance of co-locating communication and navigation payloads on a single satellite platform was highlighted in [30], optimizing resource sharing like time, frequency, and beam resources. ICAN's role in enhancing TA estimation for maintaining OFDM uplink orthogonality and reducing ICI in LEO satellites was detailed in [13]. Reid *et al.* [7] and Racelis *et al.* [31] showed how ICAN aids navigation through rapid ephemeris transmission and addressing clock deviation issues in traditional GNSS systems. Wolf [14] discussed orbit determination, demonstrating how ICAN improves satellite tracking accuracy and timeliness. For waveform design, Ma *et al.* [15] and Davarian *et al.* [16] focused on integrating pilot and communication channels within ICAN. Zou *et al.* [17] presented the optimization of cyclic code shift keying (CCSK) signals, and Huang *et al.* [18] discussed using Multi-Carrier BOC (MC-BOC) modulation for efficient data transmission in bandwidth-limited conditions.

***Asynchronous Access Interference*** – Even with a beam footprint diameter of just 10 km, the maximum delay difference in satellite communications can reach 28.9 μs, at least 5 times longer than the CP length in 5G NR. To eliminate ISI and ICI from asynchronous transmission delays, the CP length must be extended, significantly reducing frame efficiency. To address this, recent research on Filtered Orthogonal Frequency Division Multiplexing (F-OFDM) highlights its potential for asynchronous transmission and flexible sub-band settings [20], [32]. This approach relaxes synchronization requirements, simplifying hardware and algorithm design, and streamlining transceiver processing [33]. However, synchronization errors in F-OFDM can cause OoBE and altered interference distribution, increasing analytical complexity. Existing research [20], [21] mainly focuses on F-OFDM's sensitivity to synchronization errors but often lacks quantitative results. Zhang *et al.* [34] addressed this gap with a mathematical model for F-OFDM, outlining conditions for interference-free one-tap channel equalization and providing analytical expressions for ISI and ICI. Extending these findings, Chen *et al.* [35] examined uplink interference in F-OFDM systems under non-ideal synchronization, considering carrier frequency offset (CFO) and timing offset (TO). Chen *et al.* [36] further explored uplink interference under non-ideal synchronization conditions.

## B. *Organization*

The rest of this paper is outlined as follows. Section II presents the ICAN-MSAT system model for LEO networks, focusing on the communication and navigation components, and formulates an optimization problem to balance these

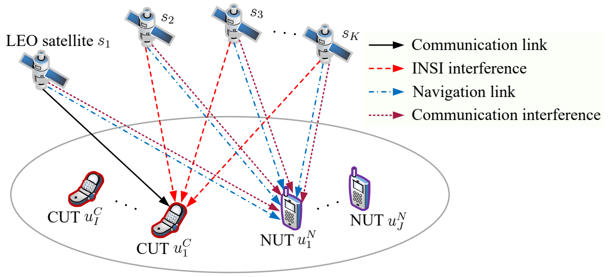

Fig. 1. Network structure of the ICAN-MSAT system.

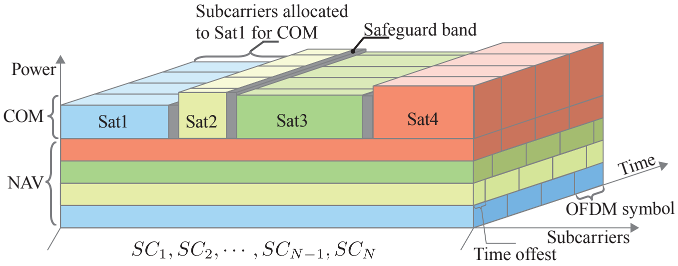

Fig. 2. Time-frequency structure of ZC-NOMA. "NAV" refers to navigation resource block and "COM" refers to communication resource block.

two aspects. Section III introduces our proposed approach for solving the optimization problem, where the PA and SA problems are addressed. The simulation results are discussed in Section IV, followed by conclusions in Section V.

### C. Notations

Boldface letters denote matrices or column vectors. The symbol $\triangleq$ defines the term on its left by the expression on its right. The operators $\exp\{\cdot\}$ and $\log\{\cdot\}$ represent exponential and logarithmic functions, respectively. The transpose of a matrix is indicated by $(\cdot)^T$ and the complex conjugate by $(\cdot)^*$. The notation $|\cdot|$ represents cardinality when applied to a set and absolute value when applied to a number. The notation $[A]_{M\times N}$ specifies that matrix or vector $A$ has dimensions of $M$ rows by $N$ columns. The set difference $\mathcal{K}\setminus\{k\}$ denotes all indices in $\mathcal{K}$ excluding $k$. Expectation and trace operations are denoted by $\mathbb{E}\{\cdot\}$ and $\mathrm{Tr}\{\cdot\}$, respectively. Finally, the $\ell_2$-norm of a vector is expressed as $\|\cdot\|_2$ and the indicator function $\mathbf{1}(\cdot)$ equals 1 if the condition inside the parentheses is true, and 0 otherwise.

## II. SYSTEM MODEL AND PROBLEM FORMULATION

### A. System Model

Consider an ICAN-MSAT system featuring joint multi-satellite transmission, as shown in Fig. 1. This system includes multiple satellites, denoted by $\boldsymbol{s} = \{\boldsymbol{s}_1, \boldsymbol{s}_2, \cdots, \boldsymbol{s}_K\}$, where $K$ is the number of satellites. On the ground, the system serves $J$ NUTs, represented as $\boldsymbol{u}^N = \{\boldsymbol{u}_1^N, \boldsymbol{u}_2^N, \cdots, \boldsymbol{u}_J^N\}$ with $\mathcal{J} = \{1, 2, \cdots, J\}$, and $I$ CUTs, denoted by $\boldsymbol{u}^C = \{\boldsymbol{u}_1^C, \boldsymbol{u}_2^C, \cdots, \boldsymbol{u}_I^C\}$ with $\mathcal{I} = \{1, 2, \cdots, I\}$. The position vectors the $k$th satellite, the $i$th CUT, and the $j$th NUT are $\boldsymbol{s}_k = (s_{x,k}, s_{y,k}, s_{z,k})^T$, $\boldsymbol{u}_i^C = (u_{x,i}^C, u_{y,i}^C, u_{z,i}^C)^T$, and $\boldsymbol{u}_j^N = (u_{x,j}^N, u_{y,j}^N, u_{z,j}^N)^T$, respectively. In the downlink scenario, every NUT receives ICAN signals from all visible satellites for navigation, while each CUT associates with at least one satellite for communication. Unique to the proposed ICAN-MSAT system, CUTs can dynamically select their access satellites and subcarriers, enhancing communication flexibility and redundancy.

In this system, the ICAN waveform transmitted by LEO satellites is Zadoff-Chu Non-Orthogonal Multiple Access (ZC-NOMA) proposed in our previous work [22], and its time-frequency structure with $K = 4$ and $N$ subcarriers is shown in Fig. 2, with $\mathcal{N} = \{1, 2, \cdots, N\}$ denoting the set of subcarrier indices.

Fig. 2 illustrates signals from four satellites using four distinct colors. Taking $\boldsymbol{s}_k$ as an example, its communication component occupies a dedicated sub-band $SB_k$, composed of subcarriers $\{SC_{n_k}, SC_{n_k+1}, \cdots, SC_{n_k+N_k-1}\}$, where $SC_n$ represents the $n$th subcarrier, $n_k$ is the starting index of the subcarriers, and $N_k$ denotes the number of carriers included in $SB_k$. Sub-bands allocated to different satellites are independent, with a guard band (GB) between them. To suppress OoBE and effectively reduce INSI during asynchronous multi-satellite access by CUTs, a filtering process similar to that implemented in F-OFDM [20], [32] is applied before signal transmission. This process is complemented by corresponding matched filtering at the receiver, allowing different satellites to transmit ICAN signals at any time without synchronization. In contrast, the navigation component of $\boldsymbol{s}_k$ is distinct from its communication counterpart. Each satellite's navigation component utilizes all subcarriers, while the communication component occupies only a portion. The navigation sequence of satellite $\boldsymbol{s}_k$ is a Zadoff-Chu (ZC) sequence of length $N$ with a unique initial root $\mu_k$, used to distinguish different satellites. This ZC sequence occupies all $N$ subcarriers and maintains a uniform power. Navigation signals $x_{\mu_k}(n)$ are time-domain waveforms formed by applying the $N$-point Inverse Discrete Fourier Transform (IDFT) to the ZC sequence with initial root $\mu_k$. The cross-correlation of navigation signals with different initial roots is approximately zero, i.e.,

$$R_{\mu_k,\mu_l}(\tau) = \sum_{n=0}^{N-1} x_{\mu_k}(n) x_{\mu_l}^*(n-\tau) \approx 0, \text{ for } \mu_k \neq \mu_l, \quad (1)$$

thereby suppressing mutual interference between the navigation signals of different satellites.

At the user end, NUTs perform time delay estimation and positioning according to the navigation signal $x_{\mu_k}(n)$, treating the communication component as interference. Conversely, CUTs rely on the embedded navigation signals within ZC-NOMA for synchronization. Once synchronized, the known navigation signal can assist the Matching Interference Cancellation (MIC), mitigating the impact of navigation components on communication components. The interference cancellation capability of $\boldsymbol{u}_i^C$ against navigation components from $\boldsymbol{s}_k$ is quantified by the interference cancellation coefficient $\alpha_{k,i}$.

We define $h_{k,n,i}^C$ as the channel coefficient from $\boldsymbol{s}_k$ to $\boldsymbol{u}_i^C$ on the $n$th subcarrier, given by $h_{k,n,i}^C = g_{k,i}^C \beta_{k,i,n}^C G_k^t G_i^{C,r}$, where $g_{k,i}^C$ represents the large-scale fading dependent on distance, $\beta_{k,i,n}^C$ represents the small-scale fading effects, $G_k^t$ is the transmit antenna gain of $\boldsymbol{s}_k$, and $G_i^{C,r}$ is the receive antenna gain of $\boldsymbol{u}_i^C$. For NUTs, the channel coefficient is analogously defined as $h_{k,n,j}^N = g_{k,j}^N \beta_{k,n,j}^N G_k^t G_j^{N,r}$, with $g_{k,j}^N$ and $\beta_{k,n,j}^N$ representing the large-scale and small-scale fading for $\boldsymbol{u}_j^N$, and $G_j^{N,r}$ as the receive antenna gain for $\boldsymbol{u}_j^N$. In addition, we define the subcarrier-to-user association coefficient set as $\boldsymbol{\delta} = \{\delta_{k,n,i} | \delta_{k,n,i} \in \{0,1\}, \forall k, n, i\}$, where $\delta_{k,n,i} = 1$ indicates that the $n$th subcarrier of $\boldsymbol{s}_k$ is associated with $\boldsymbol{u}_i^C$, and $\delta_{k,n,i} = 0$ indicates they are not associated.

### *B. Signal Model*

*1) Communication Model:* Let $\psi_{k,n,i}$ denote the signal-to-interference-plus-noise ratio (SINR) for $\boldsymbol{u}_i^C$ on the $n$th subcarrier when receiving a signal from $\boldsymbol{s}_k$, expressed as

$$\psi_{k,n,i} = \frac{p_{k,n,i}^{\mathrm{com}} \delta_{k,n,i} |h_{k,n,i}^C|^2 |F_k^t(n)|^2 |F_i^r(n)|^2}{S_{k,n,i}^C + (\sigma_{k,n,i}^C)^2}, \tag{2}$$

where $p_{k,n,i}^{\mathrm{com}}$ is the power allocated to $\boldsymbol{u}_i^C$ by $\boldsymbol{s}_k$ on subcarrier $SC_n$. $F_k^t(n)$ denotes the frequency response of the transmit filter used by $\boldsymbol{s}_k$ on $SC_n$, and $F_i^r(n)$ signifies the frequency response of the matched receive filter at $\boldsymbol{u}_i^C$ on $SC_n$. The corresponding impulse responses are represented by $f_k^t(h)$ and $f_i^r(h)$, respectively. The noise power in the system is given by $(\sigma_{k,n,i}^C)^2 = N_0 \times \Delta f$, where $N_0$ is the noise power spectral density and $\Delta f$ is the subcarrier spacing. Additionally, the total interference experienced by $\boldsymbol{u}_i^C$ during the communication with $\boldsymbol{s}_k$ on $SC_n$ is denoted by $S_{k,n,i}^C = S_{k,n,i}^{C,1} + S_{k,n,i}^{C,2}$, where $S_{k,n,i}^{C,1}$ specifically addresses the interference arising from the navigation signals of all satellites and $S_{k,n,i}^{C,2}$ describes the INSI caused by OoBE due to the asynchronous transmissions of different satellites to users. Among them, $S_{k,n,i}^{C,1}$ is given by

$$\begin{aligned} S_{k,n,i}^{C,1} = \sum_{k' \in \mathcal{K}} P_{k'}^{nav} \left| h_{k',n,i}^C \right|^2 |F_i^r(n)|^2 (1 - \alpha_{k',i}), \\ \forall k \in \mathcal{K}, i \in \mathcal{I}, n \in \mathcal{N}, \end{aligned} \tag{3}$$

where $P_{k'}^{\mathrm{nav}}$ denotes the power allocated to the navigation component on each subcarrier for $\boldsymbol{s}_{k'}$.

For $S_{k,n,i}^{C,2}$, [36] introduced a multiphase analysis method enhanced by a time-frequency transformation to tackle the challenges of interference analysis amidst imperfect synchronization. Based on [36], we solely consider the impact of TO caused by asynchronous transmission while disregarding the influence of CFO. Consequently, the expression for INSI can be given as

$$S_{k,n,i}^{C,2} = \sum_{k' \in \mathcal{K}/k} \sum_{n' \in \mathcal{N}/n} \sum_{\varrho \in \boldsymbol{\varrho}} \bar{P}_{\mathrm{ISI}_{i,kk'}^{\varrho}} \left(n, n', \Delta_{kk'}^i\right). \tag{4}$$

Define $\boldsymbol{\varrho} = \{\text{'pre'}, \text{'mid'}, \text{'post'}\}$, where the three elements corresponds to three types of interference, i.e., pre-, mid-, and post-interference. Pre-interference affects the beginning of a transmission block due to signal overlapping from previous transmissions by other satellites. Mid-interference occurs in the middle of a transmission block, typically caused by the current transmission block from other satellites. Post-interference impacts the end of a transmission block, resulting from signal overlap with subsequent transmissions by other satellites. $\bar{P}_{\mathrm{ISI}_{i,kk'}^{\varrho}} \left(n, n', \Delta_{kk'}^i\right)$ represents the interference of type $\varrho$ on $\boldsymbol{u}_i^C$ while receiving a signal on $SC_n$ from $\boldsymbol{s}_k$, due to the signal transmitted on $SC_{n'}$ from $\boldsymbol{s}_{k'}$. Its mathematical representation can be generalized as [36], i.e.,

$$\begin{aligned} \bar{P}_{\mathrm{ISI}_{i,kk'}^{\varrho}} \left(n, n', \Delta_{kk'}^i\right) = \frac{1}{N^2} \sum_{i' \in \mathcal{I}} \sum_{l_1=0}^{N-1} \left| h_{k',l_1,i}^C \right|^2 \\ p_{k',n',i'}^{com} \delta_{k',n',i'} \left| \mathcal{F}\left( \boldsymbol{\Omega}_{k,k',n,n'}^{i,\varrho}, N_j', l_1 \right) \right|^2. \end{aligned} \tag{5}$$

The function $\Omega_{k,k',n,n'}^{i,\varrho}(u)$ is further detailed as

$$\begin{aligned} \Omega_{k,k',n,n'}^{i,\varrho}(u) = \tilde{F}_k^t(u) \mathcal{F}^{-1}\left( \boldsymbol{\Psi}_{k,k',n,n'}^{i,\varrho}, 3N, u \right) \\ \times \mathcal{F}\left( \mathbf{d}_{\varrho}, 3N, u - 3n' \right), \end{aligned} \tag{6}$$

where $\tilde{F}_k^t(u) = \sum_{h=0}^{3N-1} \tilde{f}_k^t(h) e^{-j2\pi uh/3N}$. In this context, $\tilde{f}_k^t(h)$ is obtained by zero-padding the original sequence $f_k^t(h)$ to a length of $3N$. Following the same procedure, the transformed sequence $\tilde{F}_i^r(u)$ can be derived from $f_i^r(h)$. The vectors $\mathbf{d}_{\varrho}$ are specific to each INSI interference component and can be constructed as $\mathbf{d}_{\mathrm{pre}} \triangleq [\underbrace{1, \cdots, 1}_{N}, 0, \cdots, 0]_{1 \times 3N}$ and $\mathbf{d}_{\{\mathrm{mid,post}\}} \triangleq [\underbrace{1, \cdots, 1}_{N+L_{CP}}, 0, \cdots, 0]_{1 \times 3N}$. Here, $L_{CP}$ denotes the length of the cyclic prefix, and the function $\Psi_{k,k',n,n'}^{i,\varrho}(g)$ is defined as

$$\Psi_{k,k',n,n'}^{i,\varrho}(g) \triangleq \mathcal{F}\left( \boldsymbol{\xi}_{kk',g}^{i,\varrho}, N, n \right), \tag{7}$$

where $\xi_{kk',g}^{i,\varrho}(l_2) \triangleq \mathcal{F}^{-1}\left( \tilde{\boldsymbol{F}}_i^r, 3N, l_2 + L_{kk'}^{i,\varrho} - g \right)$. The specific length parameters $L_{kk'}^{i,\varrho}$ is given by $L_{kk'}^{i,pre} = 2N + 2L_{CP} - \Delta_{kk'}^i$, $L_{kk'}^{i,mid} = L_{kk'}^{i,pre} - N$ and $L_{kk'}^{i,post} = 0$. Here, $\Delta_{kk'}^i = |t_{i,k} - t_{i,k'}|$ denotes the time difference in signal reception between $\boldsymbol{s}_k$ and $\boldsymbol{s}_{k'}$ by $\boldsymbol{u}_i^C$. The term $t_{i,k}$ represents the Time of Arrival (TOA) of the signal from $\boldsymbol{s}_k$ to $\boldsymbol{u}_i^C$, defined as $t_{i,k} = \frac{1}{c} \|\boldsymbol{u}_i^C - \boldsymbol{s}_k\|_2$, where $c$ is the speed of light.

It should be noted that the function

$$\mathcal{F}(\mathbf{v}, N, m) \triangleq \sum_{k=0}^{N-1} v(k) e^{-j2\pi km/N} \tag{8}$$

defines the $N$-point Discrete Fourier Transform (DFT) of vector $\mathbf{v}$, while its counterpart

$$\mathcal{F}^{-1}(\mathbf{V}, N, k) \triangleq \frac{1}{N} \sum_{m=0}^{N-1} V(m) e^{j2\pi km/N} \tag{9}$$

specifies the corresponding $N$-point IDFT.

To simplify the representation of INSI, (4) is reconstructed by introducing a term $\Gamma_{i,k \to k'}^{n \to n'}$, which encapsulates the aggregate interference contributions. The simplified one for $S_{k,n,i}^{C,2}$ is thus given by

$$S_{k,n,i}^{C,2} = \sum_{k' \in \mathcal{K}/k} \sum_{n' \in \mathcal{N}/n} \sum_{i' \in \mathcal{I}} p_{k',n',i'}^{com} \delta_{k',n',i'} \Gamma_{i,k \to k'}^{n \to n'}, \tag{10}$$

where $\Gamma_{i,k \to k'}^{n \to n'} = \frac{1}{N^2} \sum_{\varrho \in \boldsymbol{\varrho}} \sum_{u=0}^{N-1} \Omega_{k,k',n,n'}^{i,\varrho}(u)$, which quantifies the interference transfer factor, representing the impact on $\boldsymbol{u}_i^C$ while receiving a signal on $SC_n$ from $\boldsymbol{s}_k$, due to the signal transmitted on $SC_{n'}$ from $\boldsymbol{s}_{k'}$.

The communication rate of $\boldsymbol{u}_i^C$ served by $\boldsymbol{s}_k$ on $SC_n$ is determined by

$$r_{k,n,i} = \Delta f \cdot \log_2\left(1 + \psi_{k,n,i}\right). \tag{11}$$

The sum communication rate for all CUTs within the system can thus be formulated as

$$\Upsilon = \sum_{k\in\mathcal{K}} \sum_{n\in\mathcal{N}} \sum_{i\in\mathcal{I}} r_{k,n,i}. \tag{12}$$

Furthermore, the individual communication rate for each CUT is given by

$$C_i = \sum_{k\in\mathcal{K}} \sum_{n\in\mathcal{N}} r_{k,n,i}, \quad \forall i \in \mathcal{I}. \tag{13}$$

*2) Navigation Model:* The NUT $\boldsymbol{u}_j^N$ determines its position by simultaneously receiving signals from multiple satellites, treating the signals from each satellite independently due to the uncorrelated nature of TOA measurement errors. This independence allows for straightforward combination of satellite-derived ranging data. According to [37], the Squared Position Error Bound (SPEB) acts as the TOA positioning's Mean Squared Error (MSE) lower bound for $\boldsymbol{u}_j^N$, which is mathematically expressed as

$$\mathcal{P}\left(\boldsymbol{u}_j^N\right) \triangleq \mathrm{Tr}\left\{\left(\boldsymbol{J}\left(\boldsymbol{u}_j^N\right)\right)^{-1}\right\} \le \mathbb{E}\left\{\left\|\hat{\boldsymbol{u}}_j^N - \boldsymbol{u}_j^N\right\|_2^2\right\}, \tag{14}$$

where $\boldsymbol{J}(\boldsymbol{u}_j^N) = \sum_{k\in\mathcal{K}} \boldsymbol{J}_k\left(\boldsymbol{u}_j^N\right)$ represents the Fisher Information Matrix (FIM) for $\boldsymbol{u}_j^N$, encapsulating the aggregate positioning information from $K$ satellites. $\mathbb{E}\left\{\left\|\hat{\boldsymbol{u}}_j^N - \boldsymbol{u}_j^N\right\|_2^2\right\}$ denotes the expected squared Euclidean distance between the estimated and actual positions of $\boldsymbol{u}_j^N$.

The contribution of each satellite $\boldsymbol{s}_k$ to the FIM is captured by $\boldsymbol{J}_k\left(\boldsymbol{u}_j^N\right)$, which is influenced by signal strength and the geometry of the satellite-user link, defined as [37]

$$\boldsymbol{J}_k\left(\boldsymbol{u}_j^N\right) = \frac{1}{c^2}\mu_{j,k}\boldsymbol{q}_{j,k}\boldsymbol{q}_{j,k}^T, \tag{15}$$

where $\boldsymbol{q}_{j,k}$ is a unit direction vector from $\boldsymbol{u}_j^N$ towards $\boldsymbol{s}_k$, characterized by

$$\boldsymbol{q}_{j,k} = \left(\cos\phi_{j,k}\cos\theta_{j,k}, \cos\phi_{j,k}\sin\theta_{j,k}, \sin\phi_{j,k}\right)^T. \tag{16}$$

The azimuth $\theta_{j,k}$ and elevation $\phi_{j,k}$ angles, determining the orientation of $\boldsymbol{q}_{j,k}$, are given by

$$\begin{cases} \theta_{j,k} = \arctan\left(\dfrac{u_{y,j}^N - s_{y,k}}{u_{x,j}^N - s_{x,k}}\right), \\ \phi_{j,k} = \arctan\left(\dfrac{u_{z,j}^N - s_{z,k}}{\sqrt{\left(u_{x,j}^N - s_{x,k}\right)^2 + \left(u_{y,j}^N - s_{y,k}\right)^2}}\right). \end{cases} \tag{17}$$

Furthermore, the scalar $\mu_{j,k}$, representing the Equivalent Fisher Information Matrix (EFIM) of the time delay for the ranging signal from $\boldsymbol{s}_k$ to $\boldsymbol{u}_j^N$, encapsulates the combined effects of transmission power, channel conditions, interference levels, and bandwidth [38]. It is quantitatively expressed as

$$\mu_{j,k} = \sum_{n\in\mathcal{N}} \frac{4\pi^2 P_k^{nav}\left|h_{k,n,j}^N\right|^2 \left|F_k^t(n)\right|^2 \beta_{k,n}}{(\sigma_{k,n,j}^N)^2 + S_{k,n,j}^N}, \tag{18}$$

where $P_k^{nav}$ signifies the consistent navigation power across all subcarriers for $\boldsymbol{s}_k$, and $(\sigma_{k,n,j}^N)^2 = N_0 \times \Delta f$ denotes the noise power. The mean-squared bandwidth $\beta_{k,n}$, reflecting the pulse shaping function, is defined as

$$\beta_{k,n} \triangleq \frac{\int_{-\infty}^{\infty} f^2 |P_{\text{rect}}(f)|^2\, df}{\int_{-\infty}^{\infty} |P_{\text{rect}}(f)|^2\, df} = \frac{\Delta f^2}{3\pi^2}, \tag{19}$$

assuming a typical rectangular shaping function $p_{\text{rect}}(t)$ in OFDM systems with duration $T_{\text{rect}} = 1/\Delta f$, where $P_{\text{rect}}(f)$ is its corresponding Fourier transform. Moreover, $S_{k,n,j}^N$ accounts for the interference experienced by $\boldsymbol{u}_j^N$ from $\boldsymbol{s}_k$ on $SC_n$, with a significant portion arising from the communication component on the same carrier. Given the unique properties of ZC sequences, particularly their negligible cross-correlation for distinct $\mu_k$, interference from navigation signals employing different ZC sequences can be considered negligible. Consequently, the interference term for $\boldsymbol{u}_j^N$ is simplified to

$$S_{k,n,j}^N = \sum_{k'\in\mathcal{K}} \sum_{i'\in\mathcal{I}} \delta_{k,n,i} p_{k,n,i}^{com} \left|h_{k,n,j}^N\right|^2 \left|F_k^t(n)\right|^2. \tag{20}$$

### *C. Problem Formulation*

Our work aims to maximize the sum rate of all CUTs in the proposed ICAN-MSAT system. This objective is achieved by efficiently managing power of communication and navigation components and allocating subcarriers to CUTs. Let $\boldsymbol{P}_{nav} = \{p_k^{nav} | \forall k \in \mathcal{K}\}$ and $\boldsymbol{P}_{com} = \{p_{k,n,i}^{com} | \forall k \in \mathcal{K}, n \in \mathcal{N}, i \in \mathcal{I}\}$, we formulate the following optimization problem to enhance sum communication rates while ensuring robust positioning accuracy, as follows

$$\max_{\boldsymbol{P}_{nav}, \boldsymbol{P}_{com}, \boldsymbol{\delta}} \Upsilon \tag{21a}$$

$$\text{s.t. } \mathcal{P}(\boldsymbol{u}_j^N) \le \mathcal{P}^{th}(\boldsymbol{u}_j^N), \quad \forall j \in \mathcal{J}, \tag{21b}$$

$$C_i \ge C_i^{th}, \quad \forall i \in \mathcal{I}, \tag{21c}$$

$$\sum_{n\in\mathcal{N}} \sum_{i\in\mathcal{I}} \delta_{k,n,i} P_{k,n,i} + N \times P_k^{nav} \le P_k, \forall k \in \mathcal{K}, \tag{21d}$$

$$\delta_{k,n,i} \in \{0,1\}, \quad \forall i \in \mathcal{I}, j \in \mathcal{J}, k \in \mathcal{K}, \tag{21e}$$

$$\sum_{k\in\mathcal{K}} \sum_{i\in I} \delta_{k,n,i} \le 1, \quad \forall n \in \mathcal{N}, \tag{21f}$$

$$p_{k,n,i} > 0, \quad \forall k \in \mathcal{K}, n \in \mathcal{N}, i \in \mathcal{I}, \tag{21g}$$

$$p_k^{nav} > 0, \quad \forall k \in \mathcal{K}, \tag{21h}$$

$$\sum_{k\in\mathcal{K}} \sum_{n\in\mathcal{N}} \delta_{k,n,i} \le N_i^C, \quad \forall i \in \mathcal{I}, \tag{21i}$$

$$\mu_{j,k} > \Theta_j, \quad \forall k \in \mathcal{K}. \tag{21j}$$

Constraint (21b) ensures that the SPEB for NUT $\boldsymbol{u}_j^N$ remains below the threshold $\mathcal{P}^{th}(\boldsymbol{u}_j^N)$ for accurate positioning. Constraint (21c) requires the communication rates for $\boldsymbol{u}_i^C$ to exceed $C_i^{th}$ to meet quality of service (QoS) requirements. Constraint (21d) limits the total power allocated by $\boldsymbol{s}_k$ to its capacity $P_k$. Constraints (21e) and (21f) ensure the binary nature and exclusivity of subcarrier allocation, while (21g) and (21h) ensure positive power values. Constraint (21i) limits the number of subcarriers for each $\boldsymbol{u}_i^C$ to a maximum of $N_i^C$ to ensure balanced resource distribution. Lastly, Constraint (21j) requires the navigation signal strength received by $\boldsymbol{u}_j$ from $\boldsymbol{s}_k$ to be above the capture threshold $\Theta_j$.

This article has been accepted for publication in IEEE Internet of Things Journal. This is the author's version which has not been fully edited and content may change prior to final publication. Citation information: DOI 10.1109/JIOT.2025.3526154

## III. POWER AND SUBCARRIER ALLOCATION ALGORITHM

The original optimization problem poses significant challenges due to its non-convex and non-linear nature, making it difficult to find an optimal solution. To address this, we introduce the MSASP Algorithm. The proposed algorithm iteratively solves the independent subproblems of PA and SA until convergence is reached, thereby approximating the optimal solution through successive iterations. The process at the $t$th iteration can be illustrated as

$$\cdots \xrightarrow{\boldsymbol{\delta}^{t-1}} \overbrace{\underbrace{\mathrm{Prob}_1\left(\boldsymbol{\delta}^{t-1}\right)}_{\text{PA of MSASP}} \xrightarrow[\boldsymbol{P}^t_{nav}]{\boldsymbol{P}^t_{com}} \underbrace{\mathrm{Prob}_2\left(\boldsymbol{P}^t_{com}, \boldsymbol{P}^t_{nav}\right)}_{\text{SA of MSASP}}}^{\text{Iteration } t} \xrightarrow{\boldsymbol{\delta}^{t}} \cdots .$$

The PA subproblem is formulated as

$$\max_{\boldsymbol{P}_{nav}, \boldsymbol{P}_{com}} \Upsilon \tag{22a}$$

$$\text{s.t.} \quad (21\text{b}), (21\text{c}), (21\text{d}), (21\text{g}), (21\text{h}), (21\text{j}). \tag{22b}$$

Meanwhile, the SA subproblem is described as

$$\max_{\boldsymbol{\delta}} \Upsilon \tag{23a}$$

$$\text{s.t.} \quad (21\text{c}), (21\text{e}), (21\text{f}), (21\text{i}). \tag{23b}$$

Despite the decomposition into subproblems, the inherent non-linearity and non-convex characteristics of each still present considerable computational difficulties. In response, we have developed tailored algorithms for both the PA and SA subproblems to effectively solve these challenges.

### *A. PA within the MSASP Algorithm*

The power allocation subproblem is addressed subsequent to obtaining the subcarrier assignment results from the previous iteration. Given the non-convex nature of both the objective function and the constraints, we employ the D.C. approximation method [23], which reformulates the PA problem into a tractable one by transforming the objective function into a concave minus concave form. Specifically, by jointly considering (2), (11), and (12), the objective function can be written in a format of $\Upsilon = \Delta f \sum_{k\in\mathcal{K}} \sum_{n\in\mathcal{N}} \sum_{i\in\mathcal{I}} \log_2(\psi^{(1)}_{k,n,i}/\psi^{(2)}_{k,n,i})$, which can be further split into a format of logarithmic term minus logarithmic term, i.e., $\Upsilon = \Delta f \sum_{k\in\mathcal{K}} \sum_{n\in\mathcal{N}} \sum_{i\in\mathcal{I}} \log_2 \psi^{(1)}_{k,n,i} - \Delta f \sum_{k\in\mathcal{K}} \sum_{n\in\mathcal{N}} \sum_{i\in\mathcal{I}} \log_2 \psi^{(2)}_{k,n,i}$, where the expressions of $\psi^{(1)}_{k,n,i}$ and $\psi^{(2)}_{k,n,i}$ are given by (27) and (28), respectively. Hence, the revised objective function for PA can be expressed as

$$\Upsilon = T(\boldsymbol{P}_{com}, \boldsymbol{P}_{nav}) - G(\boldsymbol{P}_{com}, \boldsymbol{P}_{nav}), \tag{24}$$

where $T(\boldsymbol{P}_{com}, \boldsymbol{P}_{nav})$ and $G(\boldsymbol{P}_{com}, \boldsymbol{P}_{nav})$ denote two concave functions defined by

$$T(\boldsymbol{P}_{com}, \boldsymbol{P}_{nav}) = \sum_{k\in\mathcal{K}} \sum_{n\in\mathcal{N}} \sum_{i\in\mathcal{I}} \Delta f \log_2(\psi^{(1)}_{k,n,i}) \tag{25}$$

and

$$G(\boldsymbol{P}_{com}, \boldsymbol{P}_{nav}) = \sum_{k\in\mathcal{K}} \sum_{n\in\mathcal{N}} \sum_{i\in\mathcal{I}} \Delta f \log_2(\psi^{(2)}_{k,n,i}), \tag{26}$$

respectively. The terms $\psi^{(1)}_{k,n,i}$ and $\psi^{(2)}_{k,n,i}$ encapsulate the composite power and interference terms, contributing to the SINR, and are given by

$$\begin{aligned}\psi^{(1)}_{k,n,i} =& P^{com}_{k,i} \delta_{k,n,i} \left|h^C_{k,n,i}\right|^2 \left|F^t_k(n)\right|^2 \left|F^r_i(n)\right|^2 \\ &+ \sum_{k'\in\mathcal{K}} (1-\alpha_{k',i}) P^{nav}_{k'} \left|h^C_{k',n,i}\right|^2 \left|F^r_i(n)\right|^2 \\ &+ \sum_{k'\in\mathcal{K}\setminus\{k\}} \sum_{i'\in\mathcal{I}} \sum_{n'\in\mathcal{N}} P^{com}_{k',i'} \delta_{k',n',i'} \Gamma^{n'\to n}_{i,k'\to k} \\ &+ (\sigma^C_{k,n,i})^2\end{aligned} \tag{27}$$

and

$$\begin{aligned}\psi^{(2)}_{k,n,i} =& \sum_{k'\in\mathcal{K}} (1-\alpha_{k',i}) P^{nav}_{k'} \left|h^C_{k',n,i}\right|^2 \left|F^r_i(n)\right|^2 \\ &+ \sum_{k'\in\mathcal{K}\setminus\{k\}} \sum_{i'\in\mathcal{I}} \sum_{n'\in\mathcal{N}} P^{com}_{k',i'} \delta_{k',n',i'} \Gamma^{n'\to n}_{i,k'\to k} \\ &+ (\sigma^C_{k,n,i})^2.\end{aligned} \tag{28}$$

Given the composition of (24) as the difference between two concave functions, it does not exhibit a strictly concave characteristic [23]. To overcome this challenge, we employ the first-order Taylor expansion to linearize $G(\boldsymbol{P})$, thereby simplifying the optimization process. $\widehat{G}(\boldsymbol{P}_{com}, \boldsymbol{P}_{nav})$ is linearized around the point $(\boldsymbol{P}^{t-1}_{com}, \boldsymbol{P}^{t-1}_{nav})$ as follows

$$\begin{aligned}&\widehat{G}(\boldsymbol{P}_{com}, \boldsymbol{P}_{nav}) \approx G\left(\boldsymbol{P}^{t-1}_{com}, \boldsymbol{P}^{t-1}_{nav}\right) \\ &+ \nabla^{\top}_{com} G\left(\boldsymbol{P}^{t-1}_{com}, \boldsymbol{P}^{t-1}_{nav}\right) \cdot \left(\boldsymbol{P}_{com} - \boldsymbol{P}^{t-1}_{com}\right) \\ &+ \nabla^{\top}_{nav} G\left(\boldsymbol{P}^{t-1}_{com}, \boldsymbol{P}^{t-1}_{nav}\right) \cdot \left(\boldsymbol{P}_{nav} - \boldsymbol{P}^{t-1}_{nav}\right).\end{aligned} \tag{29}$$

Here, the gradient vectors $\nabla^{\top}_{com}$ and $\nabla^{\top}_{nav}$ represent the partial derivatives of $G$ with respect to $\boldsymbol{P}_{com}$ and $\boldsymbol{P}_{nav}$, transposed to row vectors.

The gradient components are computed as

$$\frac{\partial G(\boldsymbol{P}_{com}, \boldsymbol{P}_{nav})}{\partial p^{com}_{k,n}} = \sum_{k'\in\mathcal{K}\setminus\{k\}} \sum_{n'\in\mathcal{N}} \sum_{i'\in\mathcal{I}} \Delta f \frac{\sum\limits_{i\in\mathcal{I}} \delta_{k,n,i} \Gamma^{n\to n'}_{i,k\to k'}}{\psi^{(2)}_{k',n',i'} \ln(2)} \tag{30}$$

and

$$\frac{\partial G(\boldsymbol{P}_{com}, \boldsymbol{P}_{nav})}{\partial P^{nav}_{k}} = \sum_{k'\in\mathcal{K}} \sum_{i'\in\mathcal{I}} \sum_{n'\in\mathcal{N}} \Delta f \frac{(1-\alpha_{k,i'})|h^C_{k,n',i'}|^2}{\psi^{(2)}_{k',n',i'} \ln(2)}. \tag{31}$$

Consequently, the optimization problem originally presented in (24) is reformulated to

$$\Upsilon = T(\boldsymbol{P}_{com}, \boldsymbol{P}_{nav}) - \widehat{G}(\boldsymbol{P}_{com}, \boldsymbol{P}_{nav}). \tag{32}$$

The same strategy is applied to constraint (21c) to handle the non-convexity. Specifically, we reformulate the constraint as

$$T_{2,i}\left(\boldsymbol{P}_{com}, \boldsymbol{P}_{nav}\right) - \widehat{G}_{2,i}\left(\boldsymbol{P}_{com}, \boldsymbol{P}_{nav}\right) > C^{th}_i, \forall i \in \mathcal{I}, \tag{33}$$

where

$$T_{2,i}\left(\boldsymbol{P}_{com}, \boldsymbol{P}_{nav}\right) = \sum_{k\in\mathcal{K}} \sum_{n\in\mathcal{N}} \Delta f \log_2\left(\psi^{(1)}_{k,n,i}\right), \forall i \in \mathcal{I} \tag{34}$$

and

$$\begin{aligned}\widehat{G}_{2,i}(\boldsymbol{P}_{com},\boldsymbol{P}_{nav}) \approx\, & G_{2,i}\left(\boldsymbol{P}_{com}^{t-1},\boldsymbol{P}_{nav}^{t-1}\right) \\ & + \nabla_{com}^{\top} G_{2,i}\left(\boldsymbol{P}_{com}^{t-1},\boldsymbol{P}_{nav}^{t-1}\right)\cdot\left(\boldsymbol{P}_{com}-\boldsymbol{P}_{com}^{t-1}\right) \\ & + \nabla_{nav}^{\top} G_{2,i}\left(\boldsymbol{P}_{com}^{t-1},\boldsymbol{P}_{nav}^{t-1}\right)\cdot\left(\boldsymbol{P}_{nav}-\boldsymbol{P}_{nav}^{t-1}\right)\end{aligned} \tag{35}$$

with

$$G_{2,i}(\boldsymbol{P}_{com},\boldsymbol{P}_{nav})=\sum_{k\in\mathcal{K}}\sum_{n\in\mathcal{N}}\Delta f \log_2\left(\psi_{k,n,i}^{(2)}\right), \forall i\in\mathcal{I}. \tag{36}$$

Differentiating $G_{2,i}\left(\boldsymbol{P}_{com},\boldsymbol{P}_{nav}\right)$ with respect to $p_{k,n,i}^{com}$ and $P_k^{nav}$, we obtain

$$\begin{aligned}&\frac{\partial G_{2,i}(\boldsymbol{P}_{com},\boldsymbol{P}_{nav})}{\partial p_{k,n}^{com}} = \\ &\sum_{k'\in\mathcal{K}\backslash\{k\}}\sum_{n'\in\mathcal{N}}\Delta f\frac{\sum\limits_{i'\in\mathcal{I}}\delta_{k,n,i'}\Gamma_{i',k\to k'}^{n\to n'}}{\psi_{k',n',i}^{(2)}\ln(2)}, \quad \forall i\in\mathcal{I},\end{aligned} \tag{37}$$

and

$$\begin{aligned}&\frac{\partial G_{2,i}(\boldsymbol{P}_{com},\boldsymbol{P}_{nav})}{\partial P_{k}^{nav}} = \\ &\sum_{k'\in\mathcal{K}}\sum_{n'\in\mathcal{N}}\Delta f\frac{(1-\alpha_{k,i})\left|F_i^r(n')\right|^2\left|h_{k,n',i}^C\right|^2}{\psi_{k',n',i}^{(2)}\ln(2)}, \forall i\in\mathcal{I}.\end{aligned} \tag{38}$$

Thus, constraint (21c) has been successfully transformed into a convex constraint shown in (33).

It is observed that constraints (21b) and (21j) remain non-convex.

***Lemma*** 1: Constraint (21b) and (21j) is inherently non-convex.

***Proof***: The convexity of $\mathcal{P}(\boldsymbol{u}_j^N)$ with respect to the FIM $\boldsymbol{J}(\boldsymbol{u}_j^N)$ is evident [39], as is the linearity of $\boldsymbol{J}(\boldsymbol{u}_j^N)$ in terms of $\mu_{j,k}$. However, the relationship between $\mu_{j,k}$ and the power allocation variables $p_k^{nav}$ and $p_{k,n,i}^{com}$ is inherently non-linear due to the fractional nature of this relationship. This leads to the non-convexity of $\mu_{j,k}$ with respect to $p_k^{nav}$ and $p_{k,n,i}^{com}$. Consequently, constraint (21b) and (21j), when considered as a function of the power allocation variables, is non-convex. ■

To address the non-convex constraints, for (18), an equivalent treatment is conducted by separating the numerator and denominator of each ratio term via a quadratic transformation [40]. Let

$$A_{k,n,j}=4\pi^2 P_k^{nav}\left|h_{k,n,j}^N\right|^2\left|F_k^t(n)\right|^2\beta_{k,n} \tag{39}$$

and

$$B_{k,n,j}=S_{k,n,j}^N+\left(\sigma_{k,n,j}^N\right)^2. \tag{40}$$

At this point,

$$\mu_{j,k}=\sum_{n\in\mathcal{N}}\frac{A_{k,n,j}}{B_{k,n,j}}. \tag{41}$$

Let $y_{k,n,j}$ be the auxiliary variable that is iteratively updated with $A_{k,n,j}$ and $B_{k,n,j}$. The closed form for $y_{k,n,j}$ is considered as [40]

$$y_{k,n,j}^*=\frac{\sqrt{A_{k,n,j}}}{B_{k,n,j}}. \tag{42}$$

Consequently, constraint (21b) is reformulated as

$$\operatorname{Tr}\left\{\left(\boldsymbol{J}^*\left(\boldsymbol{u}_j^N\right)\right)^{-1}\right\}\leq\mathcal{P}^{th}(\boldsymbol{u}_j),\forall j\in\mathcal{J}. \tag{43}$$

Here,

$$\begin{aligned}\boldsymbol{J}^*(\boldsymbol{u}_j^N)=\sum_{k\in\mathcal{K}}\sum_{n\in\mathcal{N}}&(2y_{k,n,j}^*\sqrt{A_{k,n,j}} \\ &-(y_{k,n,j}^*)^2B_{k,n,j})\boldsymbol{q}_{j,k}\boldsymbol{q}_{j,k}^T,\forall j\in\mathcal{J}.\end{aligned} \tag{44}$$

Similarly, constraint (21j) is rewritten as

$$\begin{aligned}\sum_{n\in\mathcal{N}}&\left(2y_{k,n,j}^*\sqrt{A_{k,n,j}}-\left(y_{k,n,j}^*\right)^2B_{k,n,j}\right) \\ &\boldsymbol{q}_{j,k}\boldsymbol{q}_{j,k}^T>\Theta_j,\forall k\in\mathcal{K},j\in\mathcal{J}.\end{aligned} \tag{45}$$

Considering the non-convex nature of (43) caused by the term $\sqrt{A_{k,n,j}}$, we introduce a set of auxiliary variables $\boldsymbol{t}=\{t_{k,n,j}|\forall k\in\mathcal{K},n\in\mathcal{N},j\in\mathcal{J}\}$ to serve as the proxy for $\sqrt{A_{k,n,j}}$, through which we reformulate (44) as

$$\boldsymbol{J}^*(\boldsymbol{u}_j^N)=\sum_{k\in\mathcal{K}}\sum_{n\in\mathcal{N}}(2y_{k,n,j}^*t_{k,n,j}-(y_{k,n,j}^*)^2B_{k,n,j})\boldsymbol{q}_{j,k}\boldsymbol{q}_{j,k}^T, \tag{46}$$

subject to the constraint

$$t_{k,n,j}\leq\sqrt{A_{k,n,j}},\quad\forall k\in\mathcal{K},j\in\mathcal{J},n\in\mathcal{N}. \tag{47}$$

***Lemma*** 2: Under the constraint (47), (43) is a convex constraint, and there is an equivalence transformation between it and (21b).

***Proof***: Given $y_{k,n,j}^*$, the term $2y_{k,n,j}^*t_{k,n,j}-(y_{k,n,j}^*)^2B_{k,n,j}$ is affine in terms of $\boldsymbol{P}_{\text{com}}$, $\boldsymbol{P}_{\text{nav}}$, and $\boldsymbol{t}$. Considering that $\sqrt{A_{k,n,j}}$ is concave and non-decreasing, the introduction of the constraint $t_{k,n,j}\leq\sqrt{A_{k,n,j}}$ in (47) effectively bounds $t_{k,n,j}$ by $\sqrt{A_{k,n,j}}$, thereby preserving the equivalence of the transformation. Moreover, the function $f=\operatorname{tr}\{(\cdot)^{-1}\}$ is convex [39, p. 4], and with the bound imposed by (47), the reformulated constraint in (43) maintains convexity, establishing a bound-based transformation relationship with (21b). Consequently, at the optimal point denoted by $y^*$, the first-order conditions of (21b) and (43) are coincident, ensuring that the iterative process designed for (43) will converge to the same solution as that of (21b). ■

Finally, the PA problem is reformulated into a solvable convex formulation, as specified from (48a) to (48d). This problem can now be tackled by using standard convex optimization solvers, thereby finding the optimum of the original non-convex problem effectively.

$$\max_{\boldsymbol{P}_{com},\boldsymbol{P}_{nav},\boldsymbol{t}} T(\boldsymbol{P})-\widehat{G}(\boldsymbol{P}) \tag{48a}$$

$$\text{s.t.}\quad (21\text{d}),(21\text{g}),(21\text{h}),(33),(47), \tag{48b}$$

$$\begin{aligned}&\operatorname{Tr}\left\{\left(\sum_{k\in\mathcal{K}}\sum_{n\in\mathcal{N}}(2y_{k,n,j}^*t_{k,n,j}-(y_{k,n,j}^*)^2B_{k,n,j})\boldsymbol{q}_{j,k}\boldsymbol{q}_{j,k}^T\right)^{-1}\right\} \\ &\qquad\leq\mathcal{P}^{th}(\boldsymbol{u}_j),\forall j\in\mathcal{J},\end{aligned} \tag{48c}$$

$$\begin{aligned}\sum_{n\in\mathcal{N}}&\left(2y_{k,n,j}^*t_{k,n,j}-\left(y_{k,n,j}^*\right)^2B_{k,n,j}\right) \\ &\boldsymbol{q}_{j,k}\boldsymbol{q}_{j,k}^T>\Theta_j,\forall k\in\mathcal{K},j\in\mathcal{J}.\end{aligned} \tag{48d}$$

The complete PA algorithm is shown in **Algorithm** 1.

**Algorithm 1** The Proposed PA Algorithm.

```
Step 1:
Convert Equation (24) to (32)
Convert Equation (21c) to (33)
Transform (21b) to (48c) with quadratic transformation (44)
Substitute $\sqrt{A_{k,n,j}}$ in (44) with $t_{k,n,j}$ to get (46), and add constraint (47)
Step 2:
Initialize variables $p_k^{\text{nav}}$, $p_{k,n,i}^{com}$, and $t_{k,n,j}$ within the feasible domain
Repeat:
Update $\widehat{G}(\boldsymbol{P})$ with (29)
Update $\widehat{G}_2^i(\boldsymbol{P})$ with (35)
Update $y_{k,n,j}^*$ with (42)
For fixed $y_{k,n,j}^*$, update $p_k^{\text{nav}}$ , $p_{k,n,i}^{com}$, and $t_{k,n,j}$ by solving problem (48a)
Until: Convergence criterion is reached or maximum number of iterations is achieved
```

### B. SA within the MSASP Algorithm

To address the SA problem as formulated in (23a)-(23b), we introduce the DAMSA algorithm. The non-convexity of the SA problem arises due to the binary nature of the decision variables in equation (21e). To tackle this, DAMSA dynamically pairs each CUT with an optimal set of subcarriers, while adhering to the constraint in (21i) that limits $\boldsymbol{u}_i^C$ to a maximum of $N_i^C$ subcarriers. The DAMSA algorithm operates in two sequential phases: DAMSA-I, which seeks a stable match between subcarriers and CUTs within the outlined constraints, and DAMSA-II, which is invoked to find a feasible solution when DAMSA-I cannot ensure stability. By employing this heuristic approach, we can effectively handle the non-convexity introduced by the binary variables in subcarrier allocation.

While the Gale-Shapley algorithm [41] performs well in establishing stable matches, its application is limited under conditions with specific bounds, such as those appearing in the SA problem, including QoS requirements for each CUT and the upper bound on the number of subcarriers that each CUT can access. Inspired by [42], DAMSA-I is designed to overcome these limitations through a polynomial-time approach that attempts to establish stable matches between subcarriers and CUTs.

In the proposed SA algorithm, participants on both sides (i.e., subcarriers and CUTs) first evaluate potential matches. CUTs rank subcarriers based on achievable communication rates determined by channel state information (CSI) and power allocation results from the PA algorithm to form their preference lists, i.e., $UELIST_i$ for $\boldsymbol{u}_i^C$. Similarly, subcarriers rank CUTs to form their preference lists $SCLIST_n$ for $SC_n$. DAMSA-I's operation is characterized by allowing subcarriers to propose to their most preferred CUTs, which then assess these proposals against specific criteria detailed in (21c) and (21i), ensuring that each CUT's subcarrier capacity is considered and preventing over-allocation.

**Algorithm 2** DAMSA-I

```
1:  Initialization: $\forall i \in I, \Delta C(i) := C_i^{th}$ and $\boldsymbol{\nu}_i = \emptyset$;
2:  while there exists a subcarrier $SC_n$ unassigned and it has not been rejected by all CUTs in $SCLIST_n$ do
3:      Subcarrier $SCn$ proposes to the highest ranking $\boldsymbol{u}_i^C$ who has not been proposed so far in $SCLIST_n$;
4:      $\boldsymbol{\nu}_i := \boldsymbol{\nu}_i \cup \{\mathbb{C}_i(n)\}$ ▷ $\boldsymbol{u}_i^C$ accepts $SC_n$ provisionally;
5:      if $|\boldsymbol{\nu}_i| < N_i^C$ then
6:          $\Delta C(i) := \Delta C(i) - \mathbb{C}_i(n)$ ▷ $SC_n$ can be matched with $\boldsymbol{u}_i^C$ directly;
7:      else
8:          Let the lowest ranking subcarrier with $UELIST_i$ in $\boldsymbol{\nu}_i$ be $a_{i\dagger}$;
9:          $\boldsymbol{\nu}_i := \boldsymbol{\nu}_i \setminus \mathbb{C}_i(a_{i\dagger})$ ▷ $\boldsymbol{u}_i^C$ rejects subcarrier $SC_{a_{i\dagger}}$;
10:         $\Delta C(i) := \Delta C(i) - \mathbb{C}_i(n) + \mathbb{C}_i(a_{i\dagger})$;
11:         goto Step 3;
12:     end if
13: end while
14: if there exists a CUT $\boldsymbol{u}_i^C$ with $\Delta C(i) > 0$ then
15:     Report "There is no stable match";
16: else
17:     Return the outcome $\boldsymbol{\nu} = \{\boldsymbol{\nu}_i | \forall i \in \mathcal{I}\}$, which is a stable match.
18: end if
```

A key innovation within DAMSA-I is the introduction of *deficiency capacity* $\Delta C(i)$, quantifying the difference between the current data rate achieved by $\boldsymbol{u}_i^C$ with its matched subcarriers and its QoS requirement $C_i^{\text{th}}$. The deficiency capacity, alongside a pivotal invariant, ensures algorithmic stability and adherence to constraints (21c) and (21i):

$$\textbf{Invariant A:} \quad |\boldsymbol{\nu}_i| \leq N_i^C, \quad \forall i \in \mathcal{I}, \tag{49}$$

where the set $\boldsymbol{\nu}_i = \{\mathbb{C}_i(a_{i1}), \mathbb{C}_i(a_{i2}), \cdots, \mathbb{C}_i(a_{iM_i})\}$ represents the data rates for $SC_{a_{im}}$ matched with $u_i^C$. Here, $a_{im}$ signifies the index of the $m$th subcarrier that has been matched with $u_i^C$, and $M_i$ indicates the total number of subcarriers currently paired with $u_i^C$.

Invariant A ensures that the number of subcarriers matched to $\boldsymbol{u}_i^C$ does not exceed $N_i^C$. The dynamic update of $\Delta C(i)$ enables DAMSA-I to continuously optimize subcarrier allocation to meet the QoS requirements. The pseudocode in **Algorithm** 2 outlines this process in detail.

If DAMSA-I fails to achieve stable matching, DAMSA-II is performed as a heuristic alternative. Unlike DAMSA-I, DAMSA-II prioritizes meeting the minimum QoS requirements for all CUTs. It stops allocating resources to a CUT once its QoS requirement is met, ensuring fair resource distribution across all CUTs.

DAMSA-II starts with every $\boldsymbol{u}_i^C$ proposing their preferred subcarriers on their $UELIST_i$. Then, subcarriers already matched consider switching to better proposals. For each CUT, the subcarrier matching will end when the CUT's QoS threshold is met. The entire allocation process will terminate while all CUTs are adequately served or all subcarriers are allocated. Finally, the remaining subcarriers (if any) will be

This article has been accepted for publication in IEEE Internet of Things Journal. This is the author's version which has not been fully edited and content may change prior to final publication. Citation information: DOI 10.1109/JIOT.2025.3526154

**Algorithm 3** DAMSA-II

```
1: Initialization: $\mathcal{M}_{SC}(SC_n) = \emptyset, \forall n \in \mathcal{N}$, and $\mathcal{M}_{\mathcal{U}}(\boldsymbol{u}_i^C) = \emptyset, \forall i \in \mathcal{I}$
   Step 1:
2: while there are unmatched subcarriers and unsatisfied CUTs do
3:     For $\boldsymbol{u}_i^C$ with $C_i < C_i^{th}$ and $|\mathcal{M}_{\mathcal{U}}(\boldsymbol{u}_i^C)| < N_i^C$, select the first element $SC_n$ in $UELIST_i$ and remove it from the list
4:     if $\mathcal{M}_{SC}(SC_n) \neq \emptyset$ then compare $\boldsymbol{u}_i^C$ with the current matched CUT in $SCLIST_n$ and update $\mathcal{M}_{SC}(SC_n)$ if $\boldsymbol{u}_i^C$ ranks the subcarrier higher
5:     else Directly add $\boldsymbol{u}_i^C$ to $\mathcal{M}_{SC}(SC_n)$
6:     end if
7: end while
   Step 2: Remove allocated subcarriers and generate new $UELIST_i$
8: while $\bigcup_{i=1}^{I} UELIST_i \neq \emptyset$ and $\exists i \in \mathcal{I}$ with $|\mathcal{M}_{\mathcal{U}}(\boldsymbol{u}_i^C)| < N_i^C$ do
9:     for each $\boldsymbol{u}_i^C \in \boldsymbol{u}^C$ with $|\mathcal{M}_{\mathcal{U}}(\boldsymbol{u}_i^C)| < N_i^C$ do
10:        select the first element $SC_n$ in $UELIST_i$ and remove it from the list and repeat Steps 4-6
11:    end for
12: end while
13: Return matching results $\mathcal{M}_{SC}$
```

allocated to maximize the total communication rate, similar to the strategy in DAMSA-I.

The detailed operation process of DAMSA-II is depicted by **Algorithm** 3, where $\mathcal{M}_{SC}(SC_n)$ and $\mathcal{M}_{\mathcal{U}}(\boldsymbol{u}_i^C)$ represent the matching lists of $SC_n$ and $\boldsymbol{u}_i^C$, respectively.

Next, we delve into the stability and complexity of DAMSA, starting with discussions on what constitutes a stable match.

***Definition*** 1: A match $\boldsymbol{\nu}$ is considered to be blocked by an individual $\boldsymbol{u}_i^C$, if $\boldsymbol{u}_i^C$ would prefer to reject the currently matched subcarrier due to the violation of **Invariant A** or seeks a new pairing partner $SC_n$ when the the QoS requirement $C_i^{th}$ is not met [42, p. 6].

***Definition*** 2: A pair $(SC_n, \boldsymbol{u}_i^C)$ is defined as forming a blocking pair if, given other choices, both $SC_n$ and $\boldsymbol{u}_i^C$ would mutually prefer to be matched with each rather than their respective partners in the current match $\boldsymbol{\nu}$. Furthermore, a match between $SC_n$ and $\boldsymbol{u}_i^C$ is considered to be superior if it yields a higher rate for both parties compared to the rates they can achieve with their assigned partners in the existing match $\boldsymbol{\nu}$.

***Definition*** 3: A match $\boldsymbol{\nu}$ is considered to be stable if there is no individual subcarrier/CUT or subcarrier-CUT pair thereof having the desire or incentive to change their current pairing partner within the matching context $\boldsymbol{\nu}$ [42, p. 7].

Based on Definitions 1, 2, and 3, the stabilities and complexities of DAMSA-I and DAMSA-II are further analyzed as follows.

***Theorem*** 1: The DAMSA-I algorithm is capable of producing stable match or conforming its absence with a complexity of $O(N \times I)$. Should a stable match not be feasible, DAMSA-II provides a viable alternative within the same complexity.

***Proof***: The DAMSA-I algorithm is operated by letting a CUT accept the pairing proposals from all subcarriers with **Invariant A** being assured. When the number of subcarriers allocated to CUT $\boldsymbol{u}_i^C$ reaches the maximum value $N_i^C$, $\boldsymbol{u}_i^C$ checks all the subcarriers matched with it according to its preference list. It tries to replace the least favorite one of its matched subcarriers with those subcarriers that want to match with it but have not matched with it in a one-by-one manner. If such a replacement can further improve the CUT's overall data rate, the new subcarrier will be added into the subcarrier matching list of the CUT and the least favorite one will be removed. Otherwise, the least favorite subcarrier will still be kept in the matching list. This process continues until the subcarrier matching list of CUT $\boldsymbol{u}_i^C$ does not change. If a subcarrier $SC_n$ is rejected by all of its preferable CUTs, it indicates that those CUTs have been matched with more favorite subcarriers and no blocking pair exists.

Furthermore, upon completion of the algorithm, if all CUTs have met their minimum QoS requirements, it indicates that there are no individual blockers, which means that the conditions for a stable match are satisfied as defined. Conversely, if there exists any CUT that does not meet the QoS requirements, it indicates the existence of individual blockers, which prevents DAMSA-I algorithm from achieving a stable match.

The complexity of DAMSA-I is primarily determined by the number of performed pairing operations. Each subcarrier proposes pairing requests to CUTs according to its preference list and CUTs decide whether to accept these pairing proposals or not. Since each subcarrier proposes pairing request to each CUT for only once, i.e., the pairing attempt for each subcarrier and each CUT is only performed once, checking the preference lists of all subcarriers, the total performed pairing operations (attempts) will be $O(N \times I)$. In the situations that a CUT has matched with the allowed maximum number of subcarriers, the CUT considers to replace only the least favorite one of its matching subcarriers with each of the subcarriers that have not matched with it. For a CUT, each replacement check between any two subcarriers is performed only once, thus the algorithm's overall complexity will be kept the same when such situations are involved. It is worth noting the iterative replacement process for CUTs is constrained by the limit $N_i^C$ of the allowed number of subcarriers, which ensures that the total number of comparisons remains bounded and does not exceed the order of $O(N \times I)$. Therefore, the overall complexity of DAMSA-I can be considered as $O(N \times I)$.

Analyzing the operation of DAMSA-II, we can identify that its matching process actually is similar to that of DAMSA-I. Each CUT tries to pair with each subcarrier for only once in both Step 1 and Step 2 of DAMSA-II, leading to the its overall complexity kept also at $O(N \times I)$. In addition, DAMSA-II leverages the QoS constraints to terminate the matching process for each CUT once its minimum requirements are met, which helps maintain efficiency even under high-dimensional input conditions. ■

In contrast, an exhaustive searching approach, which evaluates every possible combination of up to $N_i^C$ subcarriers for each CUT to find the highest-rate combination, corresponds to very high complexity. This approach requires assessing

This article has been accepted for publication in IEEE Internet of Things Journal. This is the author's version which has not been fully edited and content may change prior to final publication. Citation information: DOI 10.1109/JIOT.2025.3526154

TABLE I
Major Parameters Used in Simulations

| Parameter | Value |
|---|---|
| Carrier frequency ($f_c$) | 12 GHz |
| Speed of light ($c$) | $3 \times 10^8$ m/s |
| Number of OFDM subcarriers ($N$) | $\{16, 20, 24, 28\}$ |
| OFDM carrier spacing ($\Delta f$) | 15 KHz |
| Boltzmann constant ($k_{\mathrm{B}}$) | $1.38 \times 10^{-23}$ J/K |
| The noise temperature ($T_{\mathrm{n}}$) | 290 K [44] |
| Cyclic prefix length in OFDM ($L_{cp}$) | $N/4$ |
| Antenna gain ($G_k^t, G_i^{C,r}, G_j^{N,r}$) | 14, 0, 0 dBi |
| Orbit altitude ($H_s$) | 500 km |
| Radius of Earth ($R_e$) | 6371 km |
| Radius of satellites distribution plane ($R_s$) | 600 km |
| Number of satellites ($K$) | 4 |
| Satellite transmit power ($P_k$) | $\{46, 48, 50, 52, 54\}$ dBm |
| Elevation angle ($\varepsilon_0$) | 10° |
| Navigation capture threshold ($\Theta_j$) | -10 dB |
| Max subcarriers per CUT ($N_i^C$) | 5 |

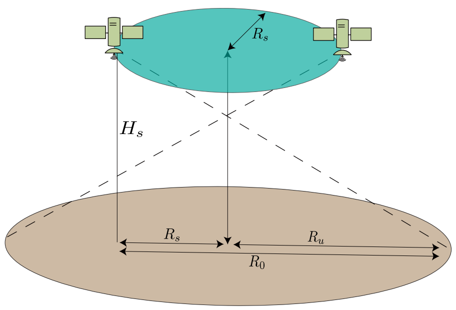

Fig. 3. Multi-satellite coverage area geometry.

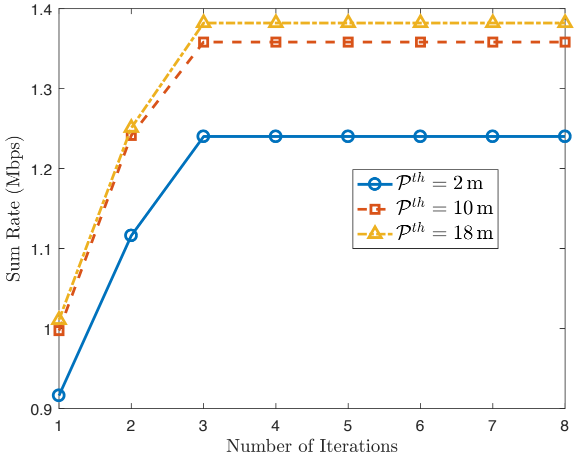

Fig. 4. Convergence performance vs. the number of iterations, where $N = 16$, $I = 6$, $J = 6$ $P_k = 48$ dBm, $\alpha_{k,i} = 0.98$, $C_i^{th} = 100$ kbps, and filter type is Hamming.

$\sum_{n'=0}^{N_i^C} \binom{N}{n'}$ combinations for each CUT, leading to an overall complexity of $O\left(\sum_{I \in \mathcal{I}} \sum_{n'=0}^{N_i^C} \binom{N}{n'}\right)$. This comparison underscores the computation efficiency of the proposed DAMSA algorithm in solving the SA problem. The significant reduction from combinatorial growth to linear complexity highlights the practical scalability of DAMSA-I and DAMSA-II, particularly for systems with a large number of subcarriers and CUTs.

## IV. Performance Evaluation

In this section, the efficiency of MSASP algorithm for the ICAN-MSAT system is evaluated via simulations. We assume a satellite network scenario involving four LEO satellites (i.e., $K = 4$) deployed with a same orbit altitude of 500 km. To ensure visibility, the elevation angle $\varepsilon_0$ of each satellite is set no less than 10 degrees. The entire system is assumed to work on Ku-band [43]. Other major parameters used in the simulations are listed in Table I. As it requires that at least four satellites should be simultaneously visible for a ground user to perform navigation and positioning, we assume that all CUTs and NUTs are deployed in an area concurrently covered by the four satellites.

The radius of a LEO satellite's ground coverage area, i.e., $R_0$, can be expressed as [45]:

$$R_0 = \sin(90^\circ - \arcsin(\frac{R_e}{R_e + H_s}\cos\varepsilon_0) - \varepsilon_0)R_e, \qquad (50)$$

where $R_e$ denotes the Earth radius and $H_s$ denotes the altitude of a LEO satellite. According to (50), when $\varepsilon_0 = 10^\circ$, $R_0$ is 1547 km.

Fig.3 shows the common coverage area of multiple satellites. When $K$ satellites are distributed within a plane with a radius of $R_s$, the radius of the common coverage area is $R_u$. The central projection points of the two planes overlap with each other, yielding $R_u = R_0 - R_s$. Therefore, when CUTs and NUTs are distributed within circular area with a radius $R_u$ of 947 km, each of them can connect to all the $K$ satellites simultaneously.

Assuming $\Delta f = 15$ kHz, the number of CUTs is required to be fewer than the number of subcarriers. In contrast, the ICAN-MSAT system imposes no stringent limit on the number of NUTs, as navigation signals are broadcast in nature. The noise power spectral density is $N_0 = k_{\mathrm{B}} T_{\mathrm{n}} = -174$ dBm/Hz.

The average convergence performance of the proposed MSASP is depicted in Fig. 4. The three curves in the figure represent the convergence behaviors of the MSASP algorithm with NUT location accuracies of 2 m, 10 m, and 18 m, respectively. It is observable that the algorithm converges rapidly within four iterations under various positioning accuracies. From the simulation process, it can be concluded that the major factors affecting the algorithm's convergence performance are the interference mitigation efficiency, the satellites' maximum transmit power, the number of users (i.e., CUTs and NUTs), and the communication and positioning requirements. Typical approaches for optimization of these conditions to speed up the algorithm's convergence include adaptive initialization method which use a well-designed initialization strategy select relatively optimal initial values to reduce the overall iterations, dynamic parameter adjustment method which can guide the algorithm toward a feasible solution more quickly by gradually relaxing QoS and positioning accuracy constraints during the initial iterations, and

This article has been accepted for publication in IEEE Internet of Things Journal. This is the author's version which has not been fully edited and content may change prior to final publication. Citation information: DOI 10.1109/JIOT.2025.3526154

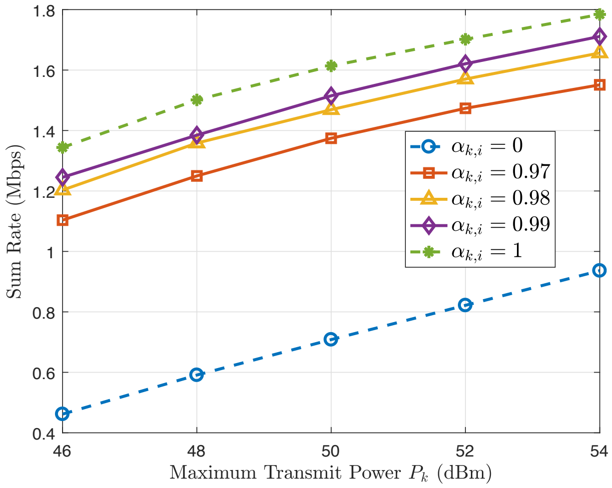

(a) Different interference mitigation factors $\alpha_{k,i}$. ($\mathcal{P}^{th} = 10$ m)

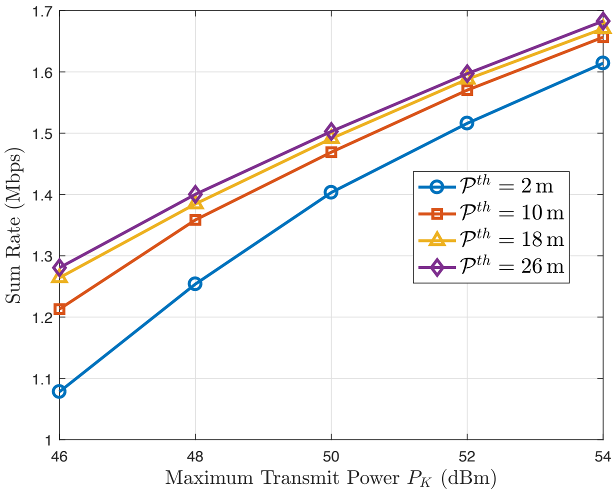

(b) Different positioning accuracies $\mathcal{P}^{th}$. ($\alpha_{k,i} = 0.98$)

Fig. 5. Performance of sum rate vs. maximum transmit power $P_k$, where $N = 16$, $I = 6$, $J = 6$, $C_i^{th} = 100$ kbps, and filter type is Hamming..

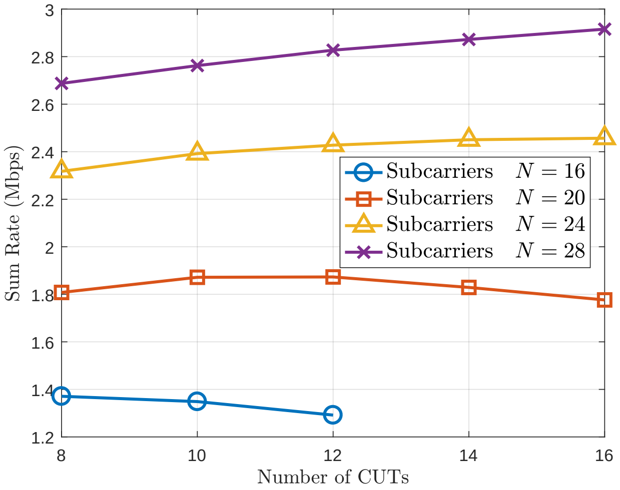

(a) CUTs ($J = 8$)

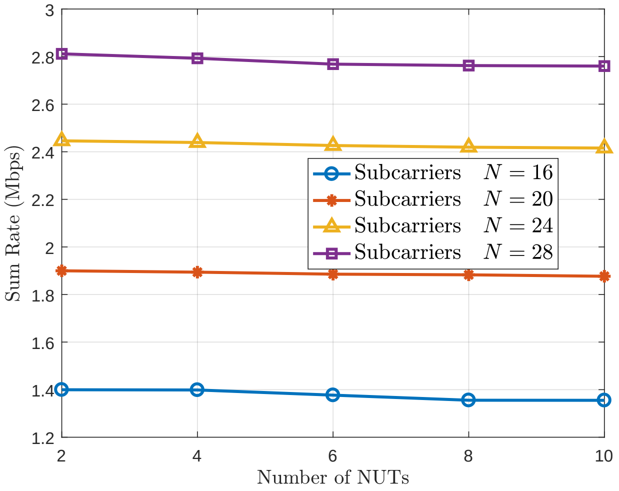

(b) NUTs ($I = 10$)

Fig. 6. Sum rate vs. numbers of CUTs and NUTs, where $P_k = 48$ dBm, $\alpha_{k,i} = 0.98$, $C_i^{th} = 100$ kbps, $\mathcal{P}^{th} = 10$ m, and filter type is Hamming.

parallel computing method which utilizes parallel processing for tasks such as subcarrier assignment and power allocation to reduce computational overhead. In this work, the first approach is adopted to achieve faster algorithmic convergence. For stricter navigation accuracy and communication constraints, an appropriate initial value selection can ensure reliable and faster algorithmic convergence.

Fig. 5 assesses the impact of the satellites' maximum transmit power $P_k$ on the sum rate for CUTs. Specifically, Fig. 5(a) demonstrates how the sum rate varies with $P_k$ under different interference mitigation factors $\alpha_{k,i}$, with two dashed lines indicating the contrasting extreme situations of $\alpha_{k,i} = 0$ and $\alpha_{k,i} = 1$. In the situation where $\alpha_{k,i} = 0$, no interference mitigation is applied to the navigation component, resulting in significant interference on CUTs. Conversely, $\alpha_{k,i} = 1$ represents an ideal condition where complete interference elimination from navigation signals is achieved, avoiding their impact on CUTs. Fig. 5(a) reveals that at $\alpha_{k,i} = 0$ with $P_k = 48$ dBm, the sum rate is as low as 0.58 Mbps, while at $\alpha_{k,i} = 1$, it increases to 1.51 Mbps. Sum rate for intermediate values of $\alpha_{k,i}$, ranging from 0.97 Mbps to 0.99 Mbps, are observed to fall between these two extremes. Under the same $P_k$, a higher $\alpha_{k,i}$ indicates a stronger interference mitigation capability for CUTs, resulting in an improved sum rate.

Fig. 5(b) explores the sum rate variability for CUTs with satellites' transmit power $P_k$ under different NUTs positioning accuracies $\mathcal{P}^{th}$. The four curves represent navigation accuracies ranging from 2 m to 26 m. With $P_k = 48$ dBm and $\mathcal{P}^{th} = 2$ m, the sum rate is 1.26 Mbps, increasing to 1.36 Mbps for $\mathcal{P}^{th} = 10$ m. As the accuracy extends to 18 m, the sum rate gain is 0.03 Mbps, with a further 0.02 Mbps gain at 26 m. These smaller increments indicate that benefits in sum rate diminish as the required positioning accuracy decreases. This trend is consistent across power levels from 46 dBm to 54 dBm, showing that lower navigation signal power in areas with lower accuracy reduces interference for CUTs. The performance under different power levels also illustrates the robustness of the MSASP algorithm across varying SNR conditions, as it consistently adapts to changes in signal strength to optimize system performance.

In Fig. 6, the variation in the sum rate with different

This article has been accepted for publication in IEEE Internet of Things Journal. This is the author's version which has not been fully edited and content may change prior to final publication. Citation information: DOI 10.1109/JIOT.2025.3526154

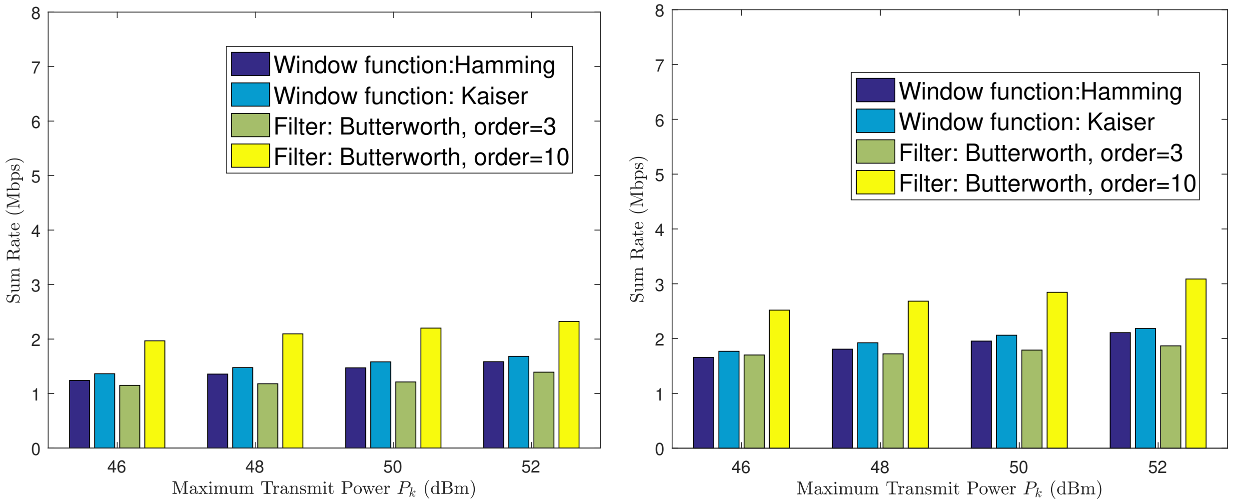

(a) $N = 16$ (b) $N = 20$

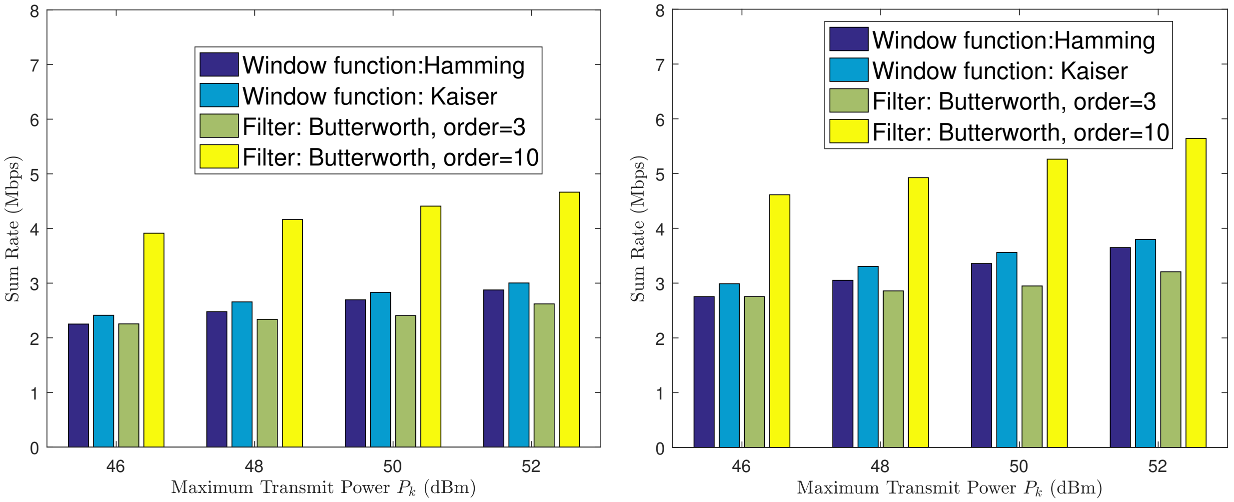

(c) $N = 24$ (d) $N = 28$

Fig. 7. The impact of filtering parameters on sum rate of CUTs, where $I = 6$, $J = 6$, $\alpha_{k,i} = 0.98$, $C_i^{th} = 100$ kbps, and $\mathcal{P}^{th} = 10$ m.

numbers of CUTs and NUTs are evaluated. Fig. 6(a) focuses on the impact of CUTs, showing that the sum rate increases significantly with the increase of $N$ when the number of CUTs is fixed. For $N = 24$ and $N = 28$, the sum rate continuously rises as the number of CUTs increases, highlighting the benefits of enhancing resource allocation flexibility. In contrast, with $N = 20$, the sum rate peaks at a specific user number and then stabilizes, indicating the limitations set by the QoS requirement $C_i^{th}$. For $N = 16$, the sum rate declines when the number of CUTs exceeds 8, with the algorithm failing to generate feasible solutions for more than 12 CUTs. This trend emphasizes the MSASP algorithm's mechanism of creating a 'guard interval', preventing the assignment of marginal subcarriers of sub-bands to CUTs. It also underscores that under stringent $C_i^{th}$, the ICAN-MSAT system can support a fewer CUTs than the total number of available subcarriers. Therefore, it is crucial to carefully balance the number of CUTs and their QoS requirements to maintain system reliability and performance.

Fig. 6(b) shows the sum rate variation for different numbers of NUTs under various number of subcarrier. For a given $N$, increasing the number of NUTs results in a gradual decrease in the sum rate due to the trade-off between navigation and communication performance. This performance degradation is subtle, unlike the more pronounced changes seen in Fig. 6(a). The subtle effect is due to the broadcast nature of navigation signals from $K$ satellites. Therefore, maintaining the same positioning accuracy $\mathcal{P}^{th}$ while serving 2 to 10 NUTs does not significantly affect the power used for navigation broadcasting or the interference level to CUTs, resulting in minimal variation in the sum rate.

The impact of different filter types and their parameters on the sum rate under different numbers of subcarriers and transmit powers are depicted in Fig. 7. These analysis involve two window functions, the Hamming and Kaiser windows, as well as Butterworth filters of third and tenth orders. Enhancements in the sum rate are consistently observed with increases in either $N$ or $P_k$, across all filters examined. Holding $P_k$ and $N$ constant, the performance of the third-order Butterworth filter ranks lowest, whereas the tenth-order Butterworth filter

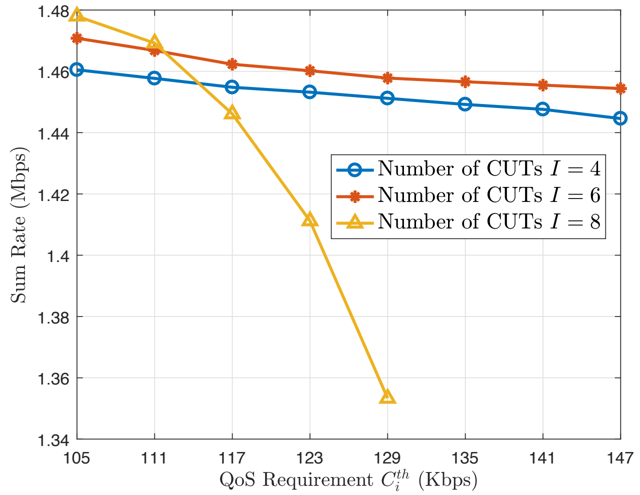

Fig. 8. Sum Rate vs. QoS requirement $C_i^{th}$ for different numbers of CUTs, where $N = 16$, $I = 6$, $J = 6$ $\alpha_{k,i} = 0.98$, $C_i^{th} = 100$ kbps, $\mathcal{P}^{th} = 10$ m, and filter type is Hamming.

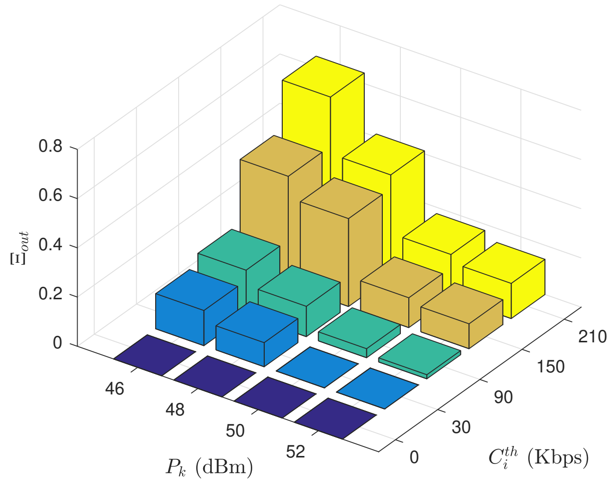

Fig. 9. Outage probability vs. satellites' transmit power and QoS requirement of CUTs, where $I = 6$, $J = 6$, $\alpha_{k,i} = 0.98$, $C_i^{th} = 100$ kbps, and $\mathcal{P}^{th} = 10$ m.

exhibits the highest performance. The enhanced performance of higher-order filters stems from their superior frequency response characteristics. Nonetheless, these benefits must be weighed against potential disadvantages such as increased complexity, higher costs, greater group delay, and phase distortion in the design phase.

Another noteworthy observation is the different impact of increasing $P_k$ on sum rate enhancements with different filters. The third-order Butterworth filter, in particular, demonstrates the slightest improvement, a situation ascribed to its less favorable frequency response configuration. As a consequence, elevations in $P_k$ do not translate into equivalent enhancements in the sum rate for this filter. Contrarily, such increases might even intensify interference with adjacent subcarriers, potentially leading to a further degradation in performance.

Fig. 8 assesses how QoS requirements $C_i^{th}$ affect the sum rate under different numbers of CUTs $I$. Observations reveal that with $C_i^{th} = 105$ kbps, increasing the number of CUTs leads to a higher sum rate, attributable to a denser user distribution that permits more flexible allocation strategies. However, as QoS requirements become more stringent, the sum rate decreases. This outcome is expected since strict QoS requirements limit the flexibility of resource allocation. Notably, at $I = 8$, unlike $I = \{4, 6\}$, a sharp sum rate decline is observed with QoS requirement increasing. This implies that for a fixed user density, there should be an upper limit of the QoS requirement. If the QoS requirement becomes larger that this limit, some communication links cannot be formed, which finally results in significant decrease on the system-wise data rate. When $C_i^{th}$ is set larger than 135 kbps, due to stringent QoS constraints, it becomes impossible to find a feasible solution. This highlights the difficulty in meeting all constraints under high QoS demands. These observations are consistent with the analysis presented for Fig. 6, showing the significant impact of QoS requirements on system performance.

To further research the impacts of satellites' maximum transmit power and QoS constraints on downlink transmissions to CUTs, a concept of transmission outage is introduced as

$$\Xi_{\text{out}} = 1 - \frac{1}{I} \sum_{i \in \mathcal{I}} \mathbf{1} \left( \sum_{k \in \mathcal{K}} \sum_{n \in \mathcal{N}} r_{k,n,i} \geq C_i^{\text{th}} \right), \tag{51}$$

which quantifies the probability that data rates for CUTs fall below the QoS requirement $C_i^{th}$.

Fig. 9 shows the outage probabilities under different transmit powers and QoS requirements. The results show that, at a fixed power level, the outage probability increases with $C_i^{th}$ increasing. Moreover, a higher transmit power level is found to be able to effectively reduce the outage probability. Nevertheless, even with a satellite transmit power of 52 dBm, there is still a significant outage probability, exceeding 10%, under stringent QoS requirements.

To evaluate the system performance under different user distribution scenarios, we consider the following five typical user distributions:

1) Random Distribution – CUTs and NUTs are randomly distributed across the coverage area.
2) Uniform Distribution – CUTs and NUTs are uniformly distributed across the coverage area.
3) Edge Distribution – CUTs and NUTs are located at the edge of the overlapping coverage area of the $K$ satellites.
4) Single-Point Concentration – All CUTs and NUTs are concentrated in a small region within the coverage area.
5) Multi-Point Concentration – Users are divided into several small groups, each concentrated in a different region within the coverage area.

Fig. 10 shows the system's sum rate performance under the five user distribution scenarios. It is seen that the user distribution significantly affects system performance. The edge distribution achieves the highest sum rate due to favorable geometric positioning relative to the $K$ satellites, minimizing the need for increased navigation power and avoiding interference with communication signals. In contrast, single-point and multi-point concentration scenarios show the lowest performance, as concentrated users tend to connect to the same satellite, limiting the benefits of multi-satellite access. Random

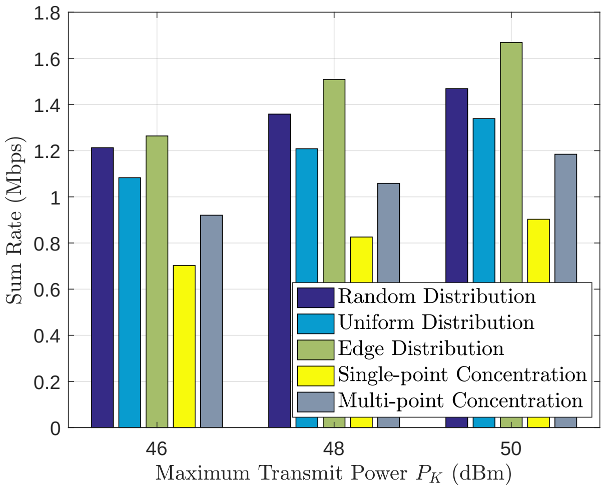

Fig. 10. Performance comparison under different user distribution scenarios, where $N = 16$, $I = 6$, $J = 6$, $\alpha_{k,i} = 0.98$, $C_i^{th} = 100$ kbps, $\mathcal{P}^{th} = 10$ m, and filter type is Hamming.

and uniform distributions perform between these extremes, with more balanced results. In summary, avoiding concentrated user distributions is key to maximizing the advantages of the ICAN-MSAT system.

Fig. 11 presents a comparative analysis of the proposed MSASP algorithm against some established benchmark algorithms in this area. These benchmarks include:

1) Bio-inspired algorithm – It employs a discrete genetic approach to iteratively solve the SA problem [46]. Its parameters are empirically determined, and for equivalence with MSASP, it solves the PA problem using a DC approximation similar to MSASP's methodology.
2) Equal power algorithm – It addresses the PA problem by ensuring a baseline navigation power, obeying the constraints in (21a), and adopts equal power allocation over communication subcarriers. The DAMSA algorithm, as introduced in this paper, is used for subcarrier allocation.
3) Baseline random algorithm – It serves as a fundamental benchmark that randomly performs power and subcarrier allocations to users without adherence to QoS or positioning accuracy constraints.

The simulation results highlight the MSASP algorithm's superior performance on sum data rates, and such a superiority is even more significant when the satellites' maximum transmit power is further increased. While the bio-inspired algorithm is capable of addressing the SA problem, it does not achieve the same level of optimization as MSASP. The equal power algorithm's simplistic uniform power distribution is inadequate when compared to the MSASP's strategy, particularly considering the prevalent INSI. The baseline random scheme, which forgoes any strategic allocation, corresponds to a performance that is significantly lagging behind, emphasizing the importance of designing efficient resource allocation strategies with assurance of both the QoS and positioning accuracy requirements. Additionally, the simulation results under different filtering configurations, as presented in Table II, further validate the adaptability and superiority of the proposed MSASP algorithm. Meanwhile, it should be noted that to ensure better performance, the proposed algorithm should be efficiently executed to adapt the network dynamics caused by user and satellite mobilities, i.e., the scheduler executing the algorithm should be able to timely acquire the network topology connection information and corresponding channel state information. If these information can not be acquired timely, the algorithms's performance will decrease.

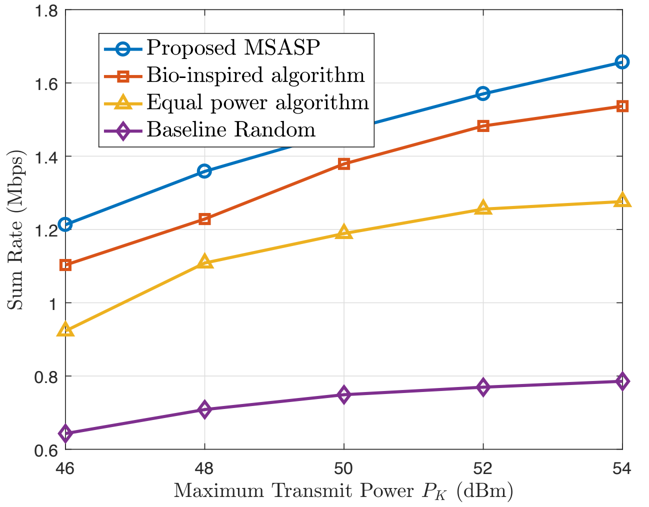

Fig. 11. Comparison of proposed MSASP scheme and existing benchmarks, where $N = 16$, $I = 6$, $J = 6$, $\alpha_{k,i} = 0.98$, $C_i^{th} = 100$ kbps, $\mathcal{P}^{th} = 10$ m, and filter type is Hamming.

TABLE II
SUM RATE PERFORMANCE OF DIFFERENT ALGORITHMS WITH VARIOUS FILTERING SCHEMES

| Filtering scheme<br>Algorithm | ⟨1⟩ | ⟨2⟩ | ⟨3⟩ | ⟨4⟩ |
|---|---|---|---|---|
| Proposed MSASP | 1.36 | 1.48 | 1.18 | 2.09 |
| Bio-inspired algorithm | 1.23 | 1.32 | 1.04 | 1.93 |
| Equal power algorithm | 1.11 | 1.19 | 0.90 | 1.83 |
| Baseline Random | 0.71 | 0.84 | 0.62 | 0.92 |

**Note**: The unit of sum rate is Mbps. ⟨1⟩ denotes Hamming filter, ⟨2⟩ denotes Kaiser filter, ⟨3⟩ denotes Butterworth filter (order = 3), and ⟨4⟩ denotes Butterworth filter (order = 10).

In practice, the deployment of ICAN-MSAT systems faces significant hardware constraints and operational challenges. The need for high-performance receivers capable of managing asynchronous transmission, real-time interference mitigation, and precise time-delay estimations introduces complexity in hardware design and increases costs. The implementation of the MSASP algorithm in a dynamic satellite environment imposes substantial computational demands, particularly for real-time resource allocation. As the number of satellites, users, and subcarriers increases, the computational complexity grows significantly, potentially leading to slower convergence, increased latency, and reduced responsiveness without advanced parallel processing. Limited memory capacity and communication bandwidth may exacerbate these issues, impacting system throughput and navigation accuracy, especially in dynamic LEO environments where CSI changes rapidly. To address these challenges, it is crucial to align hardware capabilities with system scale, optimize resource allocation processes, and explore scalable hardware architectures to ensure the system achieves the expected levels of efficiency and reliability in large-scale deployments. Furthermore, security and privacy are critical considerations in the ICAN-MSAT system. Considering the sensitivity of communication and navigation data, the ICAN-MSAT system could employ encryption techniques to secure data transmission, utilize spread spectrum and frequency hopping methods to enhance resilience against interference, and adopt signal integrity verification mechanisms to detect and mitigate spoofing attempts. To ensure privacy, strategies such as data minimization, which limits data collection to essential information, and anonymization, which prevents the direct association of user identities with the collected data, could also be explored.

## V. CONCLUSIONS

In this paper, we developed an ICAN-MSAT framework for LEO networks. We established the communication and navigation models under a multi-satellite asynchronous transmission scenario, based on which we formulate the involved joint power and subcarrier allocation issue into a mathematical optimization problem, aiming to design an efficient resource allocation scheme to manage systemic interference to enable simultaneous communication and navigation. We addressed the non-convex optimization problem by decomposing it into PA and SA subproblems. For PA, we employed D.C. programming and quadratic transformations to convert the non-convex problem into a convex one, facilitating optimal solutions. For SA, we proposed a two-stage algorithm to seek stable subcarrier-user matches and used a heuristic approach when a stable match is unattainable. Numerical results validated that our algorithm effectively supports both communication and navigation with satisfactory performance, outperforming other benchmark algorithms.

## REFERENCES

[1] P. K. Enge, "The Global Positioning System: Signals, measurements, and performance," *Int J Wireless Inf Networks*, vol. 1, no. 2, pp. 83–105, 1994.

[2] R. M. Ferre and E. S. Lohan, "Comparison of MEO, LEO, and Terrestrial IoT Configurations in Terms of GDOP and Achievable Positioning Accuracies," *IEEE Journal of Radio Frequency Identification*, vol. 5, no. 3, pp. 287–299, 2021.

[3] M. Kato, T. K. Rodrigues, T. Abe, and T. Suganuma, "Exploiting Radio Frequency Characteristics With a Support Unmanned Aerial Vehicle to Improve Wireless Sensor Location Estimation Accuracy," *IEEE Internet of Things Journal*, Early Access, 2024, doi: 10.1109/JIOT.2024.3448394.

[4] Y. Zhu, B. Mao, and N. Kato, "On a Novel High Accuracy Positioning with Intelligent Reflecting Surface and Unscented Kalman Filter for Intelligent Transportation Systems in B5G," *IEEE Journal on Selected Areas in Communications*, vol. 42, no. 1, pp. 68–77, Jan. 2024.

[5] Y. Zhu, B. Mao, and N. Kato, "IRS-Aided High Accuracy Positioning for Autonomous Driving Towards 6G: A Tutorial," *IEEE Vehicular Technology Magazine*, vol. 19, no. 1, pp. 85–92, Mar. 2024.

[6] T. G. Reid, A. M. Neish, T. F. Walter, and P. K. Enge, "Leveraging Commercial Broadband LEO Constellations for Navigating," in *The 29th International Technical Meeting of the Satellite Division of the Institute of Navigation (ION GNSS+ 2016)*, 2016, pp. 2016–16.

[7] T. G. R. Reid, A. M. Neish, T. Walter, and P. K. Enge, "Broadband LEO Constellations for Navigation," *NAVIGATION, Journal of the Institute of Navigation*, vol. 65, no. 2, pp. 205–220, 2018.

[8] T. G. R. Reid, T. Walter, P. K. Enge, D. Lawrence, H. Cobb, G. Gutt, M. O'Conner, and D. Whelan, "Navigation from Low Earth Orbit: Part 1: Concept, Current Capability, and Future Promise," *Position, Navigation, and Timing Technologies in the 21st Century: Integrated Satellite Navigation, Sensor Systems, and Civil Applications*, vol. 2, pp. 1359–1379, 2020.

[9] D. Lawrence, H. Cobb, G. Gutt, M. O'Connor, T. Reid, and T. Walter, "Navigation from LEO: Current Capability and Future Promise," *GPS World Magazine*, vol. 28, no. 7, pp. 42–48, 2017.

[10] K. Celikbilek, Z. Saleem, R. M. Ferre, J. Praks, and E. S. Lohan, "Survey on Optimization Methods for LEO-Satellite-Based Networks with Applications in Future Autonomous Transportation," *Sensors*, vol. 22, no. 4, 2022.

[11] Z. Deng, J. Mo, B. Jia, and X. Bian, "An Acquisition Scheme Based on a Matched Filter for Novel Communication and Navigation Fusion Signals," *Sensors*, vol. 17, no. 8, 2017.

[12] L. Yin, J. Cao, K. Lin, Z. Deng, and Q. Ni, "A Novel Positioning-Communication Integrated Signal in Wireless Communication Systems," *IEEE Wireless Communications Letters*, vol. 8, no. 5, pp. 1353–1356, 2019.

[13] W. Wang, T. Chen, R. Ding, G. Seco-Granados, L. You, and X. Gao, "Location-Based Timing Advance Estimation for 5G Integrated LEO Satellite Communications," *IEEE Transactions on Vehicular Technology*, vol. 70, no. 6, pp. 6002–6017, 2021.

[14] R. Wolf, "Satellite Orbit and Ephemeris Determination Using Inter Satellite Links," Ph.D. dissertation, Univ. der Bundeswehr, München, 2001.

[15] S. Ma, X. Li, and D. Zou, "A CCSK Based Navigation and Communication Integrated Satellite Signal," in *2021 International Wireless Communications and Mobile Computing (IWCMC)*, 2021, pp. 1079–1082.

[16] F. Davarian, S. Asmar, M. Angert, J. Baker, J. Gao, R. Hodges, D. Israel, D. Landau, N. Lay, and L. Torgerson, "Improving Small Satellite Communications and Tracking in Deep Space - A Review of the Existing Systems and Technologies with Recommendations for Improvement. Part II: Small Satellite Navigation, Proximity Links, and Communications Link Science," *IEEE Aerospace and Electronic Systems Magazine*, vol. 35, no. 7, pp. 26–40, 2020.

[17] D. Zou, X. Li, and R. Ma, "A Signal Optimization Strategy for next Generation Navigation and Communication Integration Applications," *Physical Communication*, vol. 50, p. 101510, 2022.

[18] X. Huang and G. Ou, "MC-BOC: A New Modulation Technology for Integrated Navigation and Communication System," *Journal of Radio Science*, vol. 35, no. 05, pp. 762–768, 2020.

[19] R. Chen, X. Lu, and K. Yang, "Joint Resource Allocation Based on F-OFDM for Integrated Communication and Positioning System," *Communications and Networking*, Springer, 2022, pp. 91–101.

[20] J. Abdoli, M. Jia, and J. Ma, "Filtered OFDM: A New Waveform for Future Wireless Systems," *2015 IEEE 16th International Workshop on Signal Processing Advances in Wireless Communications (SPAWC)*, Jun. 2015, pp. 66–70.

[21] P. Weitkemper, J. Bazzi, K. Kusume, A. Benjebbour, and Y. Kishiyama, "Adaptive Filtered OFDM with Regular Resource Grid," *2016 IEEE International Conference on Communications Workshops (ICC)*, 2016, pp. 462–467.

[22] M. Wang, G. Liu, R. Ma, W. Zhao, and W. Kang, "A Novel Navigation-Communication Integrated Waveform for LEO Network," *IEEE Global Communications Conference (GLOBECOM)*, 2022, pp. 747–752.

[23] Y. Li, M. Sheng, Y. Sun, and Y. Shi, "Joint Optimization of BS Operation, User Association, Subcarrier Assignment, and Power Allocation for Energy-Efficient HetNets," *IEEE Journal on Selected Areas in Communications*, vol. 34, no. 12, pp. 3339–3353, 2016.

[24] A. Brown, D. Reynolds, D. Roberts, and S. Serie, "Jammer and Interference Location," *The 12th International Technical Meeting of the Satellite Division of the Institute of Navigation (ION GPS 1999)*, 1999, pp. 137–142.

[25] G. Giorgi, B. Kroese, and G. Michalak, "Future GNSS Constellations with Optical Inter-Satellite Links. Preliminary Space Segment Analyses," *2019 IEEE Aerospace Conference*, 2019, pp. 1–13.

[26] T. G. R. Reid, "Launching Xona's Ravens: Commercial Satnav from LEO," *Inside GNSS*, no. 3, pp. 17, 2022.

[27] X. Su, H. Chen, J. Zhang, T. Geng, Z. Liu, X. Xie, and Q. Li, "Navigation Performance Analysis of LEO Augmented BDS-3 Navigation Constellation," *China Satellite Navigation Conference (CSNC 2021) Proceedings*, Springer, 2021, pp. 521–530.

[28] A. Batista, E. Gomez, H. Qiao, and K. E. Schubert, "Constellation Design of a Lunar Global Positioning System Using Cubesats and

This article has been accepted for publication in IEEE Internet of Things Journal. This is the author's version which has not been fully edited and content may change prior to final publication. Citation information: DOI 10.1109/JIOT.2025.3526154

Chip-Scale Atomic Clocks," *The International Conference on Embedded Systems and Applications (ESA)*, 2012, pp. 1–4.

[29] L. Meng, J. Chen, J. Wang, and Y. Zhang, "Broadcast Ephemerides for LEO Augmentation Satellites Based on Nonsingular Elements," *GPS Solutions*, vol. 25, no. 4, pp. 1–11, 2021.

[30] W. Wang, T. Chen, R. Ding, G. Seco-Granados, L. You, and X. Gao, "Location-Based Timing Advance Estimation for 5G Integrated LEO Satellite Communications," *IEEE Transactions on Vehicular Technology*, vol. 70, no. 6, pp. 6002–6017, 2021.

[31] D. Racelis, B. Pervan, and M. Joerger, "Fault-Free Integrity Analysis of Mega-Constellation-Augmented GNSS," *The 32nd International Technical Meeting of the Satellite Division of the Institute of Navigation (ION GNSS+ 2019)*, 2019, pp. 465–484.

[32] X. Zhang, M. Jia, L. Chen, J. Ma, and J. Qiu, "Filtered-OFDM - Enabler for Flexible Waveform in the 5th Generation Cellular Networks," *IEEE Global Communications Conference (GLOBECOM)*, 2015, pp. 1–6.

[33] F. Schaich and T. Wild, "Relaxed Synchronization Support of Universal Filtered Multi-Carrier Including Autonomous Timing Advance," *The 11th International Symposium on Wireless Communications Systems (ISWCS)*, 2014, pp. 203–208.

[34] L. Zhang, A. Ijaz, P. Xiao, M. M. Molu, and R. Tafazolli, "Filtered OFDM Systems, Algorithms, and Performance Analysis for 5G and Beyond," *IEEE Transactions on Communications*, vol. 66, no. 3, pp. 1205–1218, 2018.

[35] H. Chen, J. Hua, F. Li, F. Chen, and D. Wang, "Interference Analysis in the Asynchronous F-OFDM Systems," *IEEE Transactions on Communications*, vol. 67, no. 5, pp. 3580–3596, 2019.

[36] H. Chen, J. Hua, J. Wen, K. Zhou, J. Li, D. Wang, and X. You, "Uplink Interference Analysis of F-OFDM Systems under Non-Ideal Synchronization," *IEEE Transactions on Vehicular Technology*, vol. 69, no. 12, pp. 15500–15517, 2020.

[37] Y. Shen and M. Z. Win, "Fundamental Limits of Wideband Localization - Part I: A General Framework," *IEEE Transactions on Information Theory*, vol. 56, no. 10, pp. 4956–4980, 2010.

[38] Y. Karisan, D. Dardari, S. Gezici, A. A. D'Amico, and U. Mengali, "Range Estimation in Multicarrier Systems in the Presence of Interference: Performance Limits and Optimal Signal Design," *IEEE Transactions on Wireless Communications*, vol. 10, no. 10, pp. 3321–3331, 2011.

[39] Y. Shen, W. Dai, and M. Z. Win, "Power Optimization for Network Localization," *IEEE/ACM Transactions on Networking*, vol. 22, no. 4, pp. 1337–1350, 2014.

[40] S. Kaiming and Y. Wei, "Fractional Programming for Communication Systems Part I: Power Control and Beamforming," *IEEE Transactions on Signal Processing*, vol. 66, no. 10, pp. 2616–2630, 2018.

[41] D. Gale and L. S. Shapley, "College Admissions and the Stability of Marriage," *The American Mathematical Monthly*, vol. 69, no. 1, pp. 9–15, Jan. 1962.

[42] C. Huang, "Classified Stable Matching," *The 2010 Annual ACM-SIAM Symposium on Discrete Algorithms (SODA)*, Society for Industrial and Applied Mathematics, 2010, pp. 1235–1253.

[43] 3GPP, "Study on New Radio (NR) to Support Non-Terrestrial Networks (Release 15)," Technical Report TR 38.811, Oct. 2020.

[44] K.-X. Li, L. You, J. Wang, X. Gao, C. G. Tsinos, S. Chatzinotas, and B. Ottersten, "Downlink Transmit Design for Massive MIMO LEO Satellite Communications," *IEEE Transactions on Communications*,vol. 70, no. 2, pp. 1014–1028, 2022.

[45] S. Cakaj, B. Kamo, A. Lala, and A. Rakipi, "The Coverage Analysis for Low Earth Orbiting Satellites at Low Elevation," *International Journal of Advanced Computer Science and Applications*, vol. 5, no. 6, 2014.

[46] G. Wang, Y. Shao, L.-K. Chen, and J. Zhao, "Subcarrier and Power Allocation in OFDM-NOMA VLC Systems," *IEEE Photonics Technology Letters*, vol. 33, no. 4, pp. 189–192, 2021.

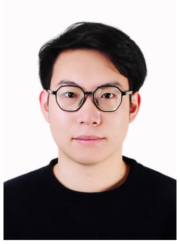

**Mingyi Wang** received his B.Sc. degree in Electronic Information Engineering from Xinjiang University, Urumqi, China, in July 2019. He is currently pursuing his Ph.D. degree in Information and Communication Engineering at Harbin Institute of Technology, China. Since August 2023, he has been a visiting researcher at Politecnico di Torino (POLITO) in Torino, Italy. His research interests include satellite communication, waveform design, channel prediction, and integrated communication and navigation.

**Ruisong Wang** received his B.Sc. degree in information and computing science from Harbin Institute of Technology, Weihai, China, in 2018. He is currently pursuing his Ph.D. degree in information and communication engineering from Harbin Institute of Technology, Harbin, China. His current research interests include underwater-overwater cooperative communications, efficient resource allocation, and satellite networks.

**Ruofei Ma** (M'14) received his B.Sc., M.Sc., and Ph.D. degrees in information and communication engineering from Harbin Institute of Technology (HIT), Harbin, China, in 2008, 2010, and 2014, respectively. From Feb. 2015 to Dec. 2016, he was a Post-Doctoral Researcher with the Department of Engineering Science, National Cheng Kung University, Taiwan. Currently, he is an associate professor in the Department of Communication Engineering, Harbin Institute of Technology, Weihai, China. His research interests include device-to-device (D2D) communications, intelligent connected-vehicles, satellite communication networks, and underwater-overwater cooperative communications and networks.

**Wenjing Kang** received her B.Sc., M.Sc., and Ph.D. degrees in measuring and control technology and instrumentations from the Harbin Institute of Technology (HIT), Harbin, China, in 2001, 2003, and 2007, respectively. She is currently an associate professor with Harbin Institute of Technology, Weihai, China. Her research interests include visual tracking and wireless networks.

**Gongliang Liu** (M'18) received his B.Sc. degree in measuring and control technology and instrumentations, and M.Sc. and Ph.D. degrees in information and communication engineering from Harbin Institute of Technology (HIT), China, in 2001, 2003, and 2007, respectively. He was a visiting scholar with the University of British Columbia, Canada, from August 2015 to August 2016. He is currently a professor at HIT, Weihai, China. His research interests are wireless communications and networks, satellite communications, and underwater communications.

**Weixiao Meng** (SM'10) received his B.Eng., M.Eng., and Ph.D. degrees from Harbin Institute of Technology (HIT), Harbin, China, in 1990, 1995, and 2000, respectively. From 1998 to 1999, he worked at NTT DoCoMo on adaptive array antenna and dynamic resource allocation for beyond 3G as a senior visiting researcher. He is now a full professor of HIT. His research interests include broadband wireless communications, space-air-ground integrated networks and wireless localization technologies. He has published 4 books and over 300 papers on journals and international conferences. He is the Chair of IEEE Communications Society Harbin Chapter, a Fellow of the China Institute of Electronics, a senior member of the IEEE ComSoc and the China Institute of Communication. He has been an editorial board member for Wiley's WCMC Journal from 2010 to 2017, an area editor for PHYCOM journal from 2014 to 2016, an editorial board for IEEE Communications Surveys and Tutorials from 2014 to 2017 and IEEE Wireless Communications since 2015. He acted as leading TPC co-chair of ChinaCom2011 and ChinaCom2016, leading Services and Applications track co-chair of IEEE WCNC2013, Awards co-chair of IEEE ICC2015 and Wireless Networking Symposia co-Chair of IEEE Globecom2015, AHSN Symposia co-Chair of IEEE Globecom2018, leading Workshop co-Chair of IEEE ICC2019 and IEEE ICNC2020, AHSN Symposia co-Chair of IEEE ICC2020. In 2005 he was honored provincial excellent returnee and selected into New Century Excellent Talents (NCET) plan by Ministry of Education (MOE), China in 2008, and the Distinguished Academic Leader of Harbin. Under his leading, Harbin Chapter won IEEE ComSoc Chapter of the Year Award and Asia Pacific Region Chapter Achievement Award, and he won Member & Global Activities Contribution Award in 2018.